Source Localization for Extremely Large-Scale Antenna Arrays under Spatial Non-Stationarity and Near-Field Effects

Xiaohuan Wu, *Member, IEEE,* Jin Qiu, Ji Sun, Wei Liu, *Senior Member, IEEE,* Haiyang Zhang, *Member, IEEE,* and Yonina C. Eldar, *Fellow, IEEE*

***Abstract*—To achieve ultra-high precision positioning, the extremely large-scale antenna array (ELAA), consisting of hundreds or even thousands of antenna elements, has garnered significant attention. However, due to increased antenna aperture, it inevitably encounters both near-field effects and spatial non-stationarity effects. In the near-field region, the traditional assumption of far-field plane wavefront no longer holds, necessitating consideration of spherical wave characteristics. Spatial non-stationarity arises when signals fail to reach the entire array, but instead only impinge on a subset of antennas, which is referred to as the signal's visible region (VR). Both effects cause model mismatch and therefore reduce positioning accuracy. In this paper, we introduce an exact near-field signal model in the context of ELAA. Based on this model, we prove that the steering vectors of source signals and the eigenvectors of the signal subspace become collinear as the number of antennas approaches infinity, which makes it easier to estimate the VR and source location parameters. Accordingly, we develop an estimation method to effectively extract the VR information of signals even when the VRs are discontinuous or overlapping. After obtaining the VR information, we propose three source localization methods that leverage the estimated VR and eigenvectors. Simulation results demonstrate that the proposed methods achieve high-precision localization while reducing computational complexity, thereby overcoming the model mismatch induced by near-field effects and spatial non-stationarity effects in ELAA.**

***Index Terms*—Extremely large-scale antenna array (ELAA), source localization, near-field, spatial non-stationarity, collinear, gridless method.**

This work was supported in part by National Natural Science Foundation of China under Grant 62471244, 62271267 and 62301277, in part by the NSF of Jiangsu Higher Education Institutions under Grant 23KJB510015, in part by Postgraduate Research & Practice Innovation Program of Jiangsu Province under Grant KYCX24_1193, in part by the Key Program of Marine Economy Development Special Foundation of Department of Natural Resources of Guangdong Province under Grant GDNRC[2023]24, in part by the Jiangsu Provincial Qinglan Project, in part by the open research fund of National Mobile Communications Research Laboratory, Southeast University under Grant 2025D09, in part by the Natural Science Foundation of Sichuan Province of China under Grant 2025ZNSFSC0514, and in part by the Natural Science Research Start-up Foundation of Recruiting Talents of Nanjing University of Posts and Telecommunications under Grant NY223031. *(Corresponding author: Haiyang Zhang)*

Xiaohuan Wu, Jin Qiu, Ji Sun and Haiyang Zhang are with the College of Telecommunications and Information Engineering, Nanjing University of Posts and Telecommunications, Nanjing 210003, China. Haiyang Zhang is also with the National Mobile Communications Research Laboratory, Southeast University, Nanjing 210096, China (e-mail: xiaohuanwu@njupt.edu.cn; haiyang.zhang@njupt.edu.cn).

Wei Liu is with the Department of Electrical and Electronic Engineering, The Hong Kong Polytechnic University, Hong Kong, China (e-mail: wei2.liu@polyu.edu.hk).

Y. C. Eldar is with Faculty of Mathematics and Computer Science, The Weizmann Institute of Science, Rehovot 7610001, Israel (e-mail: yonina.eldar@weizmann.ac.il).

I. Introduction

Source localization is playing an increasingly important role, particularly in applications such as autonomous driving and forthcoming sixth-generation (6G) mobile communications systems, which demand exceptionally stringent localization accuracy. Traditional small-scale antenna arrays have become inadequate to meet these requirements. Theoretically, the angular resolution is directly proportional to the physical aperture size of the antenna array. Consequently, to achieve ultra-high precision of localization, the employment of extremely large-scale antenna arrays (ELAAs), composed of hundreds or even thousands of antenna elements, has been proposed [1]–[7]. ELAAs have demonstrated significant advantages in enhancing localization accuracy compared to traditional small-scale antenna arrays. However, they inevitably bring forth new research challenges, particularly due to one key factor: near-field effects [8]. Near-field effects concern the scenario where targets are within the near-field region of the antenna array, rendering traditional far-field assumption-based models inapplicable [9]–[15]. This necessitates the adjustment or complete redesign of localization algorithms to achieve higher precision under near-field conditions.

In recent years, within the field of source localization, there have been works that have begun to explore design methods adapted to near-field propagation conditions [16]–[22]. These methods are all based on the near-field model of Fresnel approximation, which is also known as the second-order approximate model. This model employs a second-order Taylor expansion to approximate the spatial phase factor, neglecting the distance-related propagation attenuation. High precision requirements on the estimation are inherently difficult to reconcile with the approximation model. This effect becomes more pronounced as the array size increases, especially under ELAA conditions. It is worth noting that the application of such simplified models in ELAA scenarios further exacerbates the model mismatch issue, as the large array aperture of ELAA amplifies the deviations between the approximate models and the actual propagation characteristics [23], [24]. Specifically, in [23], it is pointed out that when far-field models are misapplied to ELAA near-field localization scenarios, significant positioning errors still occur even beyond the Fraunhofer distance, and these errors can be quantified by the model-mismatch error. In [24], it is further verified in extra-large multiple-input multiple-output (XL-MIMO) sys-

tems that simplified models fail to capture two core features of ELAA near-field scenarios (i.e., spatial non-stationarity and spherical wavefronts), ultimately leading to unavoidable mismatch-induced performance loss. To address this critical issue, in [25], an exact spherical wave model is introduced, using the range formula without simplification when expressing the phase term, and also considering amplitude variation. Reduction of estimation errors in angle and range is achieved, thereby enhancing the accuracy of localization [9], [26], [27].

Current research on near-field localization has explored multiple dimensions focusing on algorithm optimization and model characteristics. In [28], it focuses on the optimization of the near-field multiple signal classification (MUSIC) algorithm, addressing the rank deficiency issue of single-snapshot data in near-field scenario by proposing a preprocessing scheme that combines wave-number domain transformation and Stolt interpolation, ultimately achieving super-resolution localization of near-field targets. In [29], it introduces reconfigurable intelligent surfaces (RIS) into near-field localization to assist positioning by constructing controllable propagation paths, and derives the Cramér-Rao bound (CRB) for position and orientation estimation considering near-field spherical wavefronts, providing a benchmark reference for near-field localization performance. In [30], it further conducts a systematic review from signal modeling to processing, pointing out that large-aperture arrays expand the effective near-field region and enable range estimation using narrowband signals.

However, ELAA introduces not only near-field effects but also spatial non-stationarity effects. Spatial non-stationarity refers to the phenomenon where different subarrays of ELAA observe the same signal source with varying power levels, or even different signal sources altogether [31], [32]. Specifically, when ELAA operates in the radiative near-field regime, this non-stationarity manifests as incident wave energy being confined to specific local areas of the array, known as visibility regions (VRs). Consequently, the performance for localization of each source is constrained by its corresponding VR [33]–[35]. Notably, near-field localization under spatial non-stationarity remains unexplored, rendering the resolution of this critical challenge an urgent research priority.

While research on spatial non-stationarity in source localization is still in its infancy, some works in wireless communications has considered VR in channel estimation. Specifically, the "you only look once" (YOLO) neural network is introduced in [36] for object detection, by treating the channel as an image to achieve fast estimation of model parameters, including angle and delay detection paths and scatterer recognition in VR. However, it defines the VR as a collection of adjacent subarrays, implicitly assuming that the VR is continuous and neglecting more complex VR scenarios. In [37], near-field spatial non-stationarity is considered by utilizing block sparsity of subarrays. A structured block orthogonal matching pursuit algorithm is then proposed for effective active user detection and channel estimation. The sparsity of subarrays and spatial stationarity of subarray channels are exploited to design a decentralized channel estimation algorithm [38], while a VR detection algorithm is proposed by approximating the VR as a combination of subarrays of ELAA [39]. These methods divide ELAA into subarrays and assume spatial stationarity within each subarray, thereby overlooking the significant randomness of VR, as even individual subarrays exhibit substantial variations in propagation characteristics across their spatial domains. Assuming that the VR of beacon users is known *a priori*, three location-based VR identification schemes are proposed in [40], taking the user's location as input and its VR index as output. However, the performance of its VR identification heavily relies on the location of beacon users. A low-overhead joint localization and channel reconstruction scheme is proposed in [41], based on which VR identification methods are developed. A subarray-based VR identification method is proposed in [42], which initially generates step functions via least squares and quantization mapping, using coarse localization estimates to determine the VR. This is followed by iterative expansion of the largest step regions and selection of the VR with minimal residual. Although these methods achieve relatively high success rates in VR identification, they are specifically developed for near-field channel estimation and not well-suited for near-field localization. Even if viable, they remain confined to continuous and non-overlapping VR scenarios. Specifically, in practical environments characterized by overlapping and discontinuous VRs, such methods inevitably result in identification failures that induce mismatched steering vector models, thereby severely degrading source discrimination capability and causing localization failure. Furthermore, even if VR information is accurately identified, the impact of spatial non-stationarity on the performance of traditional methods (such as subspace-based methods) in localization tasks remains unclear, which may lead to inaccurate angle and range estimation. Therefore, further analysis of the underlying challenges is essential.

This paper studies ELAA-enabled source localization, accounting for both near-field effects and spatial non-stationarity effects. We first prove the collinearity between the steering vectors of source signals and the signal subspace eigenvectors. In our prior work [43], it is shown that the signal subspace eigenvectors are approximately collinear with the steering vectors, but the proof is only applicable to the case of two signals. Here, we provide a different proof, which not only clarifies the conditions for collinearity but also extends the result to scenarios with multiple signals. Specifically, we demonstrate that as the number of antennas increases, the signal subspace eigenvectors become exactly collinear with the steering vectors. Leveraging this property, we accurately estimate the VRs of each source, even when they are discontinuous or overlapping. Based on the VR information, we develop three localization algorithms to estimate both the angle and range of each source. The contributions of this paper are summarized as follows:

1) *Exact Near-Field Modeling for ELAA:* By incorporating a selection matrix to characterize the exact ELAA near-field model, the traditional Fresnel approximation is avoided and spatial non-stationarity and near-field effects are more accurately represented. Moreover, problem and challenges faced by applying the MUSIC algorithm within the exact ELAA near-field model are analyzed.

This article has been accepted for publication in IEEE Transactions on Signal Processing. This is the author's version which has not been fully edited and content may change prior to final publication. Citation information: DOI 10.1109/TSP.2026.3654842

2) *Collinearity Establishment in ELAA:* By analyzing the relationship between the eigenvectors within the signal subspace of the covariance matrix and each steering vector, we prove that in ELAA scenario, each eigenvector exhibits unique collinearity with one steering vector. This property is applicable to a variety of complex scenarios ranging from spatial stationarity to spatial non-stationarity, and from non-overlapping VRs to overlapping VRs.
3) *Collinearity-Based Source Localization:* A novel VR estimation method is proposed based on the collinearity property, ensuring effectiveness in complex scenarios with overlapping or discontinuous VRs. Building on this, three localization algorithms, which include a correlation localization algorithm, a MUSIC-based localization algorithm, and a gridless localization algorithm, are proposed considering both speed and accuracy. Specifically, the first two effectively reduce computational complexity while ensuring high-precision localization estimation, whereas the third further improves positioning accuracy and reduces computational overhead through efficient gridless search.

The rest of this paper is organized as follows. Section II presents the exact near-field model with spatial non-stationarity in ELAA scenario. In Section III, the challenges encountered in applying MUSIC to ELAA scenario are discussed, and the collinearity between steering vectors and eigenvectors is analyzed. A VR estimation method and three algorithms for angle and range estimation are presented in Section IV. Simulations conducted in Section V validate the collinearity theorem and demonstrate the proposed solutions' superiority in angle and range estimation, achieving significant improvements in both positioning accuracy and computational complexity. Finally, conclusions are drawn in Section VI.

We adopt the following notations throughout this paper. The set of complex numbers is denoted by $\mathbb{C}$. The conjugate transpose of a matrix $\boldsymbol{A}$ is represented by $\boldsymbol{A}^H$. An identity matrix of dimension $N \times N$ is expressed as $\boldsymbol{I}_N$. The ℓ_2-norm of a matrix $\boldsymbol{A}$ is written as $\|\boldsymbol{A}\|_2$, while a diagonal matrix whose diagonal entries correspond to the elements of vector $\boldsymbol{x}$ in sequence is denoted as $\mathrm{diag}(\boldsymbol{x})$. The inner product between vectors $\boldsymbol{a}$ and $\boldsymbol{b}$ is defined as $\langle \boldsymbol{a}, \boldsymbol{b} \rangle$.

II. System Model

In this section, we introduce the signal model of ELAA considering both the exact steering vector and spatial non-stationarity.

A. Exact Signal Model

As shown in Fig. 1, consider an M-element uniform linear array (ULA) where M is very large (e.g., hundreds or thousands of antennas). We set the reference point at the center of the array and the index set of the antennas is denoted as $\boldsymbol{\phi} = \left\{-\frac{M-1}{2}, \cdots, \frac{M-1}{2}\right\}$. The spacing between two adjacent antennas is d. In ELAA, the large array aperture leads to a large Rayleigh distance, which is defined as the boundary that separates near-field and far-field regions of the array. The Rayleigh distance is calculated as $2D^2/\lambda$, where D denotes the array aperture and λ is the signal wavelength. For example, when the carrier frequency is 300GHz, the Rayleigh distance of a 512-element ULA is 131 meters. If the ULA has 1000 elements, this distance extends to 500 meters. Therefore, some sources may lie within the near-field region of ELAA, necessitating the use of spherical wave modeling to accurately characterize the impinging signal propagation, instead of plane wave approximation.

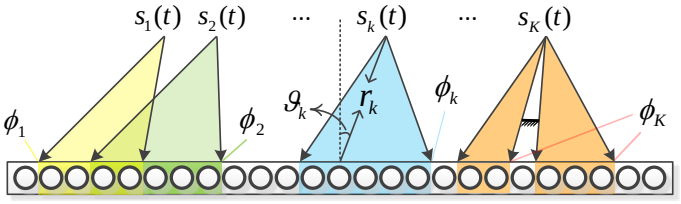

Fig. 1. Spatial non-stationarity of K sources in ELAA, where the VRs of different sources are highlighted by different colors and they may be discontinuous or overlapping, or both.

We assume K narrowband near-field uncorrelated source signals impinge onto the array. The position of the k-th source is denoted by $\{\vartheta_k, r_k\}$, where ϑ_k is the angle of the k-th source and r_k the range between the reference point and the k-th source. The signal received by the m-th antenna is [25]

$$y_m(t) = \sum_{k=1}^{K} a_m(\vartheta_k, r_k) s_k(t) + n_m(t), \tag{1}$$

where $a_m(\vartheta_k, r_k) = \frac{r_k}{r_{m,k}} e^{-j\frac{2\pi}{\lambda}(r_{m,k} - r_k)}$, $s_k(t)$ is the k-th narrowband signal, λ is the wavelength of the signal, $n_m(t)$ is additive white Gaussian noise with zero mean and $r_{m,k}$ is the range between the m-th antenna and the k-th source defined as,

$$\begin{aligned} r_{m,k} &= \sqrt{(md - r_k \sin(\vartheta_k))^2 + (r_k \cos(\vartheta_k))^2} \\ &= \sqrt{r_k^2 - 2 r_k m d \sin(\vartheta_k) + (md)^2}. \end{aligned} \tag{2}$$

B. Spatial Non-Stationarity

In ELAA, with the increase of array aperture, different sources may only "see" a portion of the array, as shown in Fig. 1, where different colors indicate the VRs of different sources. These VRs may be discontinuous or overlapping, or both. When VRs are discontinuous, they may consist of two or more discontinuous subarrays that collectively receive signals. When there are overlapping regions, the antennas in the overlapping region can receive two or more signals simultaneously, whereas the non-overlapping regions are restricted to receiving only a single signal each. Formally, the VR of the k-th source is denoted as $\boldsymbol{\phi}_k$ which consists of the indices of the antennas observed by the k-th source. Then, $\boldsymbol{\phi}_k \subseteq \boldsymbol{\phi}$, and $\boldsymbol{\phi}_k = \boldsymbol{\phi}$ indicates spatial stationarity. To incorporate spatial non-stationarity into model (1), we introduce a selection matrix $\boldsymbol{\Gamma} = [\boldsymbol{\gamma}_1, \cdots, \boldsymbol{\gamma}_K] \in \{0,1\}^{M \times K}$ where the m-th element in $\boldsymbol{\gamma}_k$ is

$$(\boldsymbol{\gamma}_k)_m = \begin{cases} 1, & m \in \boldsymbol{\phi}_k \\ 0, & \text{otherwise.} \end{cases} \tag{3}$$

For example, for $M = 7$ and $K = 3$, we have $\boldsymbol{\phi} = \{-3, -2, -1, 0, 1, 2, 3\}$; assume that $\boldsymbol{\phi}_1 = \{-3, -2, -1\}$,

This article has been accepted for publication in IEEE Transactions on Signal Processing. This is the author's version which has not been fully edited and content may change prior to final publication. Citation information: DOI 10.1109/TSP.2026.3654842

$\boldsymbol{\phi}_2 = \{-2,-1,0,1\}$ and $\boldsymbol{\phi}_3 = \{-1,0,2,3\}$, so $\boldsymbol{\gamma}_1 = [1,1,1,0,0,0,0]^T$, $\boldsymbol{\gamma}_2 = [0,1,1,1,1,0,0]^T$ and $\boldsymbol{\gamma}_3 = [0,0,1,1,0,1,1]^T$. Then, $\boldsymbol{\phi}_1$ and $\boldsymbol{\phi}_2$ are overlapping, and $\boldsymbol{\phi}_3$ is discontinuous. In this case,

$$\boldsymbol{\Gamma} = \begin{bmatrix} 1 & 0 & 0 \\ 1 & 1 & 0 \\ 1 & 1 & 1 \\ 0 & 1 & 1 \\ 0 & 1 & 0 \\ 0 & 0 & 1 \\ 0 & 0 & 1 \end{bmatrix}. \tag{4}$$

As a result, model (1) is replaced by

$$y_m(t) = \sum_{k=1}^{K} (\boldsymbol{\gamma}_k)_m a_m(\vartheta_k, r_k) s_k(t) + n_m(t). \tag{5}$$

The received signals of the entire array is represented by,

$$\begin{aligned} \boldsymbol{y}(t) &= \sum_{k=1}^{K} \underbrace{[\boldsymbol{\gamma}_k \circ \boldsymbol{a}(\vartheta_k, r_k)]}_{\hat{\boldsymbol{a}}(\vartheta_k, r_k)} \boldsymbol{s}(t) + \boldsymbol{n}(t) \\ &= \hat{\boldsymbol{A}} \boldsymbol{s}(t) + \boldsymbol{n}(t), \end{aligned} \tag{6}$$

where $\boldsymbol{y}(t) = [y_1(t), \cdots, y_M(t)]^T$, $\circ$ denotes the Hadamard product, $\boldsymbol{s}(t) = [s_1(t), \cdots, s_K(t)]^T$ and $\boldsymbol{n}(t) = [n_1(t), \cdots, n_M(t)]^T$ are the source and noise signals, respectively, $\boldsymbol{a}(\vartheta_k, r_k) = [a_1(\vartheta_k, r_k), \cdots, a_M(\vartheta_k, r_k)]^T$ for $k = 1, \cdots, K$, and $\hat{\boldsymbol{A}} = [\hat{\boldsymbol{a}}(\vartheta_1, r_1), \cdots, \hat{\boldsymbol{a}}(\vartheta_K, r_K)]$ is the corresponding array manifold matrix. Our primary objective is to achieve source localization through joint estimation of the angle ϑ_k and range r_k using model (6). However, as will be seen in Section III, the presence of $\boldsymbol{\gamma}_k$ introduced by the VR leads to parameter estimation errors in MUSIC. Furthermore, the steering vector $\boldsymbol{a}(\vartheta_k, r_k)$ does not possess the Vandermonde structure required by traditional gridless methods (e.g., root-MUSIC and ESPRIT), thereby rendering these algorithms inapplicable. Consequently, achieving precise source localization becomes challenging under such conditions. To address this challenge, we systematically analyze the underlying issues and propose a collinearity theorem in the subsequent sections to facilitate accurate angle and range estimation.

III. The Collinearity Property in ELAA

In this section, we provide collinearity property of ELAA which can help to accurately estimate the VR and location parameters. Specifically, in Section III-A, we show that MUSIC cannot accurately locate the sources when the VR information is unknown because MUSIC spectrum is generated based on the assumption of spatial stationarity. In Section III-B, we show that MUSIC still cannot successfully locate the sources even if the VR information is known *a priori* due to the difficulty in distinguishing signals received by overlapping regions of different VRs, as well as the issue of pseudo peaks in non-stationary scenario which is reported for the first time. To enable accurate estimation of VR and location parameters, the collinearity property of ELAA is presented in Section III-C.

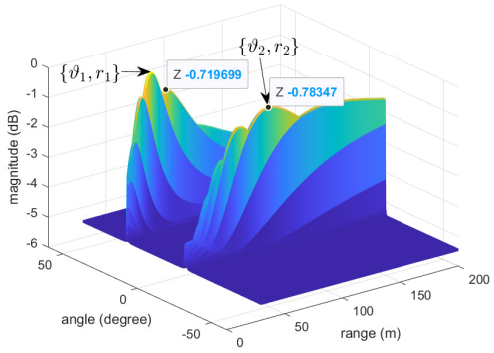

Fig. 2. The spectrum of MUSIC applying to the exact near-field model with spatial non-stationarity when $K = 2$ and the peaks of the two sources are $\{\vartheta_1, r_1\}$ and $\{\vartheta_2, r_2\}$.

A. MUSIC under Unknown VR

When the VR information is unknown, applying the MUSIC algorithm to the exact near-field model with spatial non-stationarity generates a significant number of pseudo peaks, rendering the algorithm ineffective. This occurs because MUSIC relies on steering vectors based on the assumption of spatial stationarity during the search process, rather than using the actual steering vectors that exhibit spatial non-stationarity. The use of mismatched steering vectors inevitably reduces estimation accuracy, leading to diminished spectral peak sharpness in the MUSIC algorithm, thereby impacting the algorithm's ability to resolve distinct signal sources and limiting the traditional MUSIC algorithm's estimation performance under the ELAA model. To illustrate this issue, Fig. 2 presents the MUSIC spectrum for two signals impinging on a 500-element ELAA. The simulation parameters include a signal-to-noise ratio (SNR) of 10 dB, wavelength $\lambda = 0.01m$, source parameters $\{\vartheta_1, r_1\} = \{30°, 5000\lambda\}$ with a VR spanning subarrays $\boldsymbol{\phi}_1 = \{1, \cdots, 360\}$, and $\{\vartheta_2, r_2\} = \{-10°, 10000\lambda\}$ with $\boldsymbol{\phi}_2 = \{171, \cdots, 500\}$. As shown, two peak clusters emerge, each containing multiple peaks. The highest peaks of the two clusters are denoted as $\{\vartheta_1, r_1\}$ and $\{\vartheta_2, r_2\}$, respectively. Notably, the magnitude of the highest pseudo peak, i.e., the second highest peak, in the left cluster (-0.719699) exceeds that of the highest peak in the right cluster (-0.78347), making it difficult to identify the position of the main peak represented by $\{\vartheta_2, r_2\}$. In addition, the shapes of the two peak clusters are not sharp enough, which can also have a negative impact on our judgment of the main peak, especially when the SNR is low. Therefore, to enhance estimation accuracy, it is necessary to consider VR information, thus improving the effectiveness of the MUSIC algorithm under the ELAA model.

B. MUSIC under Known VR

Although recovering VR information prior to applying the MUSIC algorithm for angle and range estimation is theoretically feasible, due to the necessity of conducting multiple grid searches, the computation load will increase significantly. Furthermore, this approach also encounters two critical challenges. On the one hand, the VRs of different

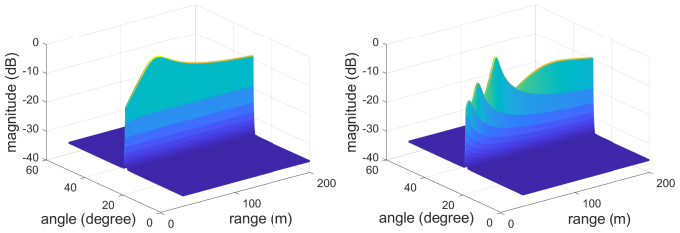

(a) $\boldsymbol{\phi} = \{201, \cdots, 300\}$ (b) $\boldsymbol{\phi} = \{151, \cdots, 250\}$

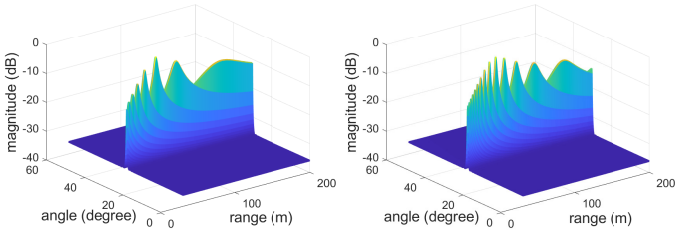

(c) $\boldsymbol{\phi} = \{101, \cdots, 200\}$ (d) $\boldsymbol{\phi} = \{1, \cdots, 100\}$

Fig. 3. The spectrum of MUSIC when the VR center gradually shifts leftward under known VR.

signals may overlap, and therefore, even if the VRs can be accurately estimated, it is still impossible to estimate angles and ranges due to difficulty in distinguishing signals received by overlapping regions. On the other hand, even if there is no overlap among VRs, i.e., each VR only receives a single signal, we still encounter the issue of pseudo peaks, which will be illustrated below.

In traditional near-field models without spatial non-stationarity, the reference point is typically set at the array center. However, in the ELAA signal model, each of the K sources corresponds to a distinct subarray defined by $\boldsymbol{\phi}_1, \cdots, \boldsymbol{\phi}_K$. For each subarray, the reference point is not necessarily at the center of the subarray. Only when the center of the subarray is at the center of the entire array will its reference point be at the center of the subarray. To validate this, an experiment is conducted with parameters $M = 500$ and $\{\vartheta, r\} = \{30^\circ, 7000\lambda\}$. As shown in Fig. 3, when the VR center is located at the center of the array, no pseudo peaks appear. However, as the VR center deviates from the array center, pseudo peaks emerge, and the more severe the deviation from the array center, the more pseudo peaks appear, with some of them exhibiting higher amplitudes. Although pseudo peaks can be avoided by resetting the reference point of each subarray after obtaining the VR, it is difficult to achieve accurate VR estimation. When the VR estimation error is large, the pseudo peaks problem remains inevitable.

C. The Collinearity Property

In MUSIC algorithm, the covariance matrix $\boldsymbol{R}$ of the received signal $\boldsymbol{y}(t)$ can be decomposed into signal subspace $\boldsymbol{U_S}$ and noise subspace $\boldsymbol{U_N}$ by eigenvalue decomposition,

$$\boldsymbol{R} = \boldsymbol{U_S}\boldsymbol{\Sigma_S}\boldsymbol{U_S}^H + \boldsymbol{U_N}\boldsymbol{\Sigma_N}\boldsymbol{U_N}^H \tag{7}$$

where $\boldsymbol{U_S} = [\boldsymbol{v}_1, \cdots, \boldsymbol{v}_{k'}, \cdots, \boldsymbol{v}_K]$. The K eigenvectors in $\boldsymbol{U_S}$ correspond to the K largest eigenvalues $\{\lambda_{k'}\}_{k'=1}^K$. It is well-known that the space spanned by $\boldsymbol{U_S}$ and that by the array manifold $\hat{\boldsymbol{A}}$ is theoretically coincident. In traditional far-field scenario, it is not easy to find the relationship between $\hat{\boldsymbol{a}}(\vartheta_k, r_k)$ and $\boldsymbol{v}_{k'}$. However, for the exact signal model (6) in ELAA, we observe a close relationship between the two vectors, i.e., they are collinear when $M \to \infty$. To see this, we first provide the following definitions.

Definition 1: *The correlation between vectors $\boldsymbol{c}$ and $\boldsymbol{d}$ is,*

$$e_{\boldsymbol{cd}} = \frac{\left|\boldsymbol{c}\boldsymbol{d}^H\right|}{\|\boldsymbol{c}\|_2\|\boldsymbol{d}\|_2}. \tag{8}$$

Then, the two vectors are collinear if $e_{\boldsymbol{cd}} = 1$.

Theorem 1: *For the exact near-field model under ELAA, when $\{\frac{p_k n_k r_k}{\cos(\vartheta_k)}\}_{k=1}^K$ are unequal, where p_k denotes signal power of the k-th source and $n_k = \frac{\|\hat{\boldsymbol{a}}(\vartheta_k, r_k)\|_2^2}{\|\boldsymbol{a}(\vartheta_k, r_k)\|_2^2} \in (0, 1]$, the signal subspace eigenvectors $\{\boldsymbol{v}_1, \cdots, \boldsymbol{v}_K\}$ of the covariance matrix are collinear with the steering vectors $\{\hat{\boldsymbol{a}}(\vartheta_1, r_1), \cdots, \hat{\boldsymbol{a}}(\vartheta_K, r_K)\}$ as $M \to \infty$.*

Proof: See Appendix A. □

Remark 1: *Since the probability that there exists a case of equality $\{\frac{p_k n_k r_k}{\cos(\vartheta_k)}\}_{k=1}^K$ is extremely low, Theorem 1 holds true in the vast majority of scenarios. Furthermore, we will validate such a case in subsequent simulation experiments. It should be pointed out that Theorem 1 holds true regardless of the presence of spatial non-stationarity and whether VRs overlap or not. Thus, the collinearity property also exists in spatial stationary scenario when $M \to \infty$.*

By Theorem 1, we find a collinear relationship between the eigenvectors $\{\boldsymbol{v}_k\}_{k=1}^K$ and $\{\hat{\boldsymbol{a}}(\vartheta_k, r_k)\}_{k=1}^K$. Consequently, given the eigenvectors $\{\boldsymbol{v}_k\}_{k=1}^K$ of covariance matrix $\boldsymbol{R}$, obtaining the VR and source location parameters will become much easier. In the next section, we will present methods for VR estimation and source localization based on Theorem 1. It should be noted that, existing methods [36], [41] assume the VRs are continuous while we assume the VRs are arbitrary. Hence, the methods proposed in Section IV based on Theorem 1 are more applicable in complex scenarios where the VRs are discontinuous, which will also be verified in Section V.

IV. VR Estimation and Source Localization

Leveraging the collinearity property we first propose a method for VR estimation, regardless of whether the VRs of signals overlap or not, in Section IV-A. Based on the estimated VR information, we further propose three different source localization algorithms in Section IV-B, Section IV-C, and Section IV-D, respectively.

A. VR Estimation

Due to the collinearity between steering vectors and eigenvectors, the VR information of the steering vectors can be mapped onto the eigenvectors, as shown in Fig. 4. We can

This article has been accepted for publication in IEEE Transactions on Signal Processing. This is the author's version which has not been fully edited and content may change prior to final publication. Citation information: DOI 10.1109/TSP.2026.3654842

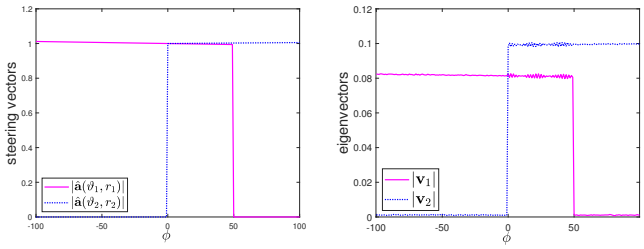

(a) $|\hat{\boldsymbol{a}}(\vartheta_1, r_1)|, |\hat{\boldsymbol{a}}(\vartheta_2, r_2)|$ (b) $|\boldsymbol{v}_1|, |\boldsymbol{v}_2|$

Fig. 4. Visualization of element-wise magnitudes of steering vectors and eigenvectors when $M = 201$, $K = 2$, $\boldsymbol{\phi}_1 = \{-100, \cdots, 50\}$, $\boldsymbol{\phi}_2 = \{0, \cdots, 100\}$.

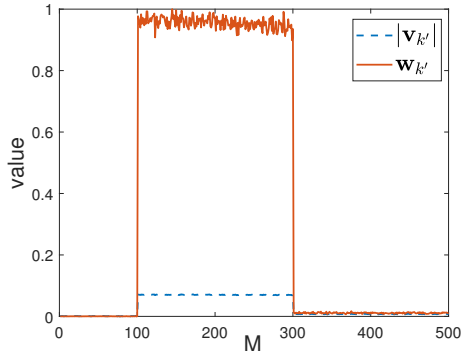

Fig. 5. Comparison between $\boldsymbol{w}_{k'}$ and $|\boldsymbol{v}_{k'}|$ when the SNR is 5 dB.

estimate VR through variations in the magnitude of eigenvectors. However, when SNR is low, noise can interfere with the estimation of VR boundaries. The most straightforward approach is to estimate the two distinct jump points on either side of each eigenvector. However, this method performs poorly in low SNR conditions due to noise interference. Therefore, we consider filtering out values outside the VR by setting a threshold, while ensuring that the values within the VR encompass most of received signal's power. This method exhibits strong robustness against fluctuating noise and has relatively low computational complexity. To further reduce the impact of noise interference, before estimation, a preprocessing step can be applied to the eigenvector: for the k'-th eigenvector $\boldsymbol{v}_{k'}$, first construct a new covariance matrix $\boldsymbol{R}_{k'} = \boldsymbol{v}_{k'}\boldsymbol{v}_{k'}^H$, and then proceed with the following steps,

$$\boldsymbol{w}_{k'} = \left[\|\boldsymbol{R}_{(k',1)}\|_2^2, \cdots, \|\boldsymbol{R}_{(k',M)}\|_2^2\right], \tag{9}$$

where $\boldsymbol{R}_{(k',m)}$ is the m-th column of $\boldsymbol{R}_{k'}$. As can be seen from Fig. 5, under the premise that the values of $\boldsymbol{w}_{k'}$ and $|\boldsymbol{v}_{k'}|$ are almost identical outside the VR, the values of $\boldsymbol{w}_{k'}$ within the VR are significantly higher than the original values of $|\boldsymbol{v}_{k'}|$. This preprocessing step addresses the issue of noise interference in low SNR conditions, enhancing the robustness against noise disturbances. This enhancement is more conducive to our approach of estimating the VR by setting thresholds. The estimated VR of the k'-th eigenvector is denoted as,

$$\tilde{\boldsymbol{\phi}}_{k'} = \left\{\tilde{\overline{\boldsymbol{N}}}_{k'}, \tilde{\overline{\boldsymbol{N}}}_{k'} + 1, \cdots, \tilde{\underline{\boldsymbol{N}}}_{k'} - 1, \tilde{\underline{\boldsymbol{N}}}_{k'}\right\}, \tag{10}$$

where $\tilde{\overline{\boldsymbol{N}}}_{k'}$ is the estimated minimum index and $\tilde{\underline{\boldsymbol{N}}}_{k'}$ is the estimated maximum one. Therefore, we obtain the selection vector of the k'-th eigenvector,

$$(\tilde{\boldsymbol{\gamma}}_{k'})_m = \begin{cases} 1, & m \in \tilde{\boldsymbol{\phi}}_{k'} \\ 0, & \text{Otherwise.} \end{cases} \tag{11}$$

B. Correlation Localization Algorithm

Since the steering vector and the eigenvector are collinear, we can leverage the correlation between these two vectors for source localization. We employ a grid search approach to identify the angle and range parameters that correspond to the largest correlation between the steering vector and the k'-th eigenvector,

$$\arg\max_{\tilde{\vartheta}, \tilde{r}} \left\langle \boldsymbol{v}_{k'} \circ \tilde{\boldsymbol{\gamma}}_{k'}, \frac{\boldsymbol{a}(\tilde{\vartheta}, \tilde{r}) \circ \tilde{\boldsymbol{\gamma}}_{k'}}{\|\boldsymbol{a}(\tilde{\vartheta}, \tilde{r}) \circ \tilde{\boldsymbol{\gamma}}_{k'}\|_2} \right\rangle, \tag{12}$$

where $\{\tilde{\vartheta}, \tilde{r}\}$ represents the grid points in angle and range spaces. This algorithm is referred to as CLA-VR in subsequent experiments.

Remark 2: *Because of large amplitude variations in the exact near-field model, it is necessary to normalize all steering vectors before calculating correlations; otherwise, it may lead to parameter estimation errors.*

C. Localization Algorithm Based on MUSIC

Conducting a global search using the MUSIC algorithm is impractical since the array size is large, so we consider reducing the dimension. For simplicity, we assume an one-to-one correspondence between the eigenvectors of the signal subspace and the steering vectors, i.e., the k-th eigenvector $\boldsymbol{v}_k$ is collinear with the k-th steering vector $\hat{\boldsymbol{a}}(\vartheta_k, r_k)$, respectively.[1] So we have,

$$\boldsymbol{v}_k = u_k \hat{\boldsymbol{a}}(\vartheta_k, r_k), \tag{13}$$

where u_k, $k = 1, \cdots, K$ are complex coefficients. Furthermore, extracting data within the VRs of $\boldsymbol{v}_k$ and ignoring data outside the VRs, we can obtain $\boldsymbol{v}_{\tilde{\boldsymbol{\phi}}_k}$, whose dimension is related to the size of their VRs. Construct the following covariance matrix for the k-th source,

$$\boldsymbol{R}_k = \boldsymbol{v}_{\tilde{\boldsymbol{\phi}}_k}\boldsymbol{v}_{\tilde{\boldsymbol{\phi}}_k}^H = u_k^2 \hat{\boldsymbol{a}}(\vartheta_k, r_k)\hat{\boldsymbol{a}}^H(\vartheta_k, r_k), \tag{14}$$

Consequently, we can directly apply MUSIC to $\boldsymbol{R}_k$ to estimate the angle and range of the k-th source. Since the size of VR may be much smaller than that of the entire array, utilizing (14) can significantly reduce the computational complexity. Therefore, this algorithm is designated as Fast MUSIC-VR in subsequent experiments.

[1]This one-to-one correspondence assumption is solely for simplifying the mathematical representation and derivation process. In practical scenarios, the collinearity relationship does not strictly follow the index matching of k. For example, the eigenvector indexed k' (e.g., $\boldsymbol{v}_1$) may be collinear with the steering vector indexed k (e.g., $\hat{\boldsymbol{a}}(\vartheta_2, r_2)$), and the indices k and k' do not necessarily correspond to each other.

Remark 3: *It should be noted that our method Fast MUSIC-VR estimates the angle and range parameters by finding the maximum value in each small-dimensional MUSIC spectrum rather than using a time-consuming full-array two-dimensional search to find K peaks. Moreover, the computational efficiency of this method is closely correlated with the size of the VR. The smaller the VR, the more efficient the Fast MUSIC-VR. Since each small-dimensional spectrum only contains the signal of a single source. Consequently, there is no need to account for the impact of pseudo peaks. The avoidance of redundant computations in peak finding thereby enables the method to achieve higher computational efficiency.*

D. Gridless Localization Algorithm

Algorithm 1 Gridless Localization Algorithm

Input: Eigenvectors $\boldsymbol{v}_1, \cdots, \boldsymbol{v}_K$, estimated VR vectors $\tilde{\boldsymbol{\gamma}}_1, \cdots, \tilde{\boldsymbol{\gamma}}_K$, iteration number T.

Output: Optimal position of the particle swarm $\boldsymbol{P}_{g,\vartheta}$, $\boldsymbol{P}_{g,r}$.

for each particle i **do**
  for each dimension d **do**
    Initialize position $\boldsymbol{\Lambda}_i$, $\boldsymbol{R}_i$ randomly within the effective near-field range;
    Initialize position $\boldsymbol{V}_{i,\vartheta}$, $\boldsymbol{V}_{i,r}$ randomly within permissible range;
  end for
end for
for each $k' \in [1, K]$ **do**
  for each particle i **do**
    Calculate the maximum fitness value $f(\vartheta_{i1}, r_{i1}, k'), \cdots, f(\vartheta_{iD}, r_{iD}, k')$ of particle based on (15);
    The optimal position for the individual corresponding to the maximum fitness value is $\boldsymbol{P}_{p,\vartheta}$, $\boldsymbol{P}_{p,r}$;
    Update $\boldsymbol{P}_{g,\vartheta}$, $\boldsymbol{P}_{g,r}$;
    if $f(\boldsymbol{\Lambda}_{i,t+1}, \boldsymbol{R}_{i,t+1}, k') < f(\boldsymbol{P}_{i,\vartheta,t}, \boldsymbol{P}_{i,r,t}, k')$ **then**
      $p^d_{i,\vartheta,t+1} = \vartheta^d_{i,t+1}$, $p^d_{i,r,t+1} = r^d_{i,t+1}$;
    else
      $p^d_{i,\vartheta,t+1} = p^d_{i,\vartheta,t}$, $p^d_{i,r,t+1} = r^d_{i,t}$;
    end if
  end for
  for each particle i **do**
    for each dimension d **do**
      $v^d_{i,\vartheta,t+1} = \omega v^d_{i,\vartheta,t} + c_1 rand\left(p^d_{i,\vartheta,t} - \vartheta^d_{i,t}\right) + c_2 rand\left(p^k_{g,\vartheta,t} - \vartheta^d_{i,t}\right)$;
      $v^d_{i,r,t+1} = \omega v^d_{i,r,t} + c_1 rand\left(p^d_{i,r,t} - r^d_{i,t}\right) + c_2 rand\left(p^k_{g,r,t} - r^d_{i,t}\right)$;
      $\vartheta^d_{i,t+1} = \vartheta^d_{i,t} + v^d_{i,\vartheta,t+1}$, $r^d_{i,t+1} = r^d_{i,t} + v^d_{i,r,t+1}$;
      Update $\boldsymbol{P}_{g,\vartheta}$, $\boldsymbol{P}_{g,r}$;
    end for
  end for
  Repeat the above steps until $t = T$;
end for

The CLA-VR and Fast MUSIC-VR proposed in Section IV-B and Section IV-C belong to on-grid algorithms which suffer from grid mismatch effect and high computational complexity issue. In order to solve this problem, we consider avoiding the grid search process to propose a gridless algorithm which utilizes the particle swarm optimization (PSO) technique to solve the non-convex optimization problem in terms of angle and range parameters. PSO is an evolutionary optimization technique, and its core idea is to use information sharing of individuals in the group to make the movement of the whole group evolve from disorder to order in the problem solving space, so as to obtain a feasible solution to the problem [44], [45]. Each individual is defined as a particle, which represents a potential solution in the search space, and it can memorize the optimal position of the group and its own optimal position and speed. In each generation, the particle information is combined to adjust the speed of each dimension, which is used to calculate the new position of the particle. The particle changes its state continuously in the multi-dimensional search space until it reaches the optimal state. In a continuous spatial coordinate system, a particle swarm can be mathematically described as follows. Let the size of the particle swarm be N, and for each particle in a D-dimensional space, its position vector is represented by $\boldsymbol{\Lambda}_{i,\vartheta} = (\vartheta_{i1}, \cdots, \vartheta_{id}, \cdots, \vartheta_{iD})$, $\boldsymbol{R}_{i,r} = (r_{i1}, \cdots, r_{id}, \cdots, r_{iD})$, and its velocity vector by $\boldsymbol{V}_{i,\vartheta} = (v_{i1,\vartheta}, \cdots, v_{id,\vartheta}, \cdots, v_{iD,\vartheta})$, $\boldsymbol{V}_{i,r} = (v_{i1,r}, \cdots, v_{id,r}, \cdots, v_{iD,r})$. The individual optimal position, i.e., the best position experienced by the particle, is denoted as $\boldsymbol{P}_{i,\vartheta} = (p_{i1,\vartheta}, \cdots, p_{id,\vartheta}, \cdots, p_{iD,\vartheta})$ and $\boldsymbol{P}_{i,r} = (p_{i1,r}, \cdots, p_{id,r}, \cdots, p_{iD,r})$, while the global optimal position, i.e., the best position experienced by any individual within the swarm is represented as $\boldsymbol{P}_{g,\vartheta} = (p_{g1,\vartheta}, \cdots, p_{gd,\vartheta}, \cdots, p_{gD,\vartheta})$ and $\boldsymbol{P}_{g,r} = (p_{g1,r}, \cdots, p_{gd,r}, \cdots, p_{gD,r})$. It is important to note that the fitness value at each position is set to be the correlation between the steering vector at that position and the k'-th eigenvector, with the specific expression being:

$$f(\vartheta_{id}, r_{id}, k') = \frac{\langle \boldsymbol{v}_{k'} \circ \tilde{\boldsymbol{\gamma}}_{k'}, \boldsymbol{a}(\vartheta_{id}, r_{id}) \circ \tilde{\boldsymbol{\gamma}}_{k'} \rangle}{\|\boldsymbol{v}_{k'} \circ \tilde{\boldsymbol{\gamma}}_{k'}\|_2 \|\boldsymbol{a}(\vartheta_{id}, r_{id}) \circ \tilde{\boldsymbol{\gamma}}_{k'}\|_2}. \quad (15)$$

Based on the PSO algorithm, the corresponding gridless localization algorithm is summarized in Algorithm 1, which is named PSO-VR in following experiments. It should be noted that the values of ω, c_1, c_2 are empirically determined through repeated experiments.

V. Simulation Results

In this section, extensive simulations are performed to validate the collinearity theorem and evaluate the performance of our proposed methods, including the VR estimation method and three localization algorithms. Unless otherwise specified, considering computational complexity, a ULA with $M = 500$ antennas[2], with its center located at the origin of the coordinate system, is employed. The inter-element spacing $d = \lambda/2$, where the wavelength of the signal $\lambda = 0.01m$, and the number of snapshots $L = 2000$. Since the near-field region

[2]In fact, our method shows better performance in larger arrays. However, implementing traditional methods such as MUSIC requires significant amount of time. Hence, we set $M = 500$.

This article has been accepted for publication in IEEE Transactions on Signal Processing. This is the author's version which has not been fully edited and content may change prior to final publication. Citation information: DOI 10.1109/TSP.2026.3654842

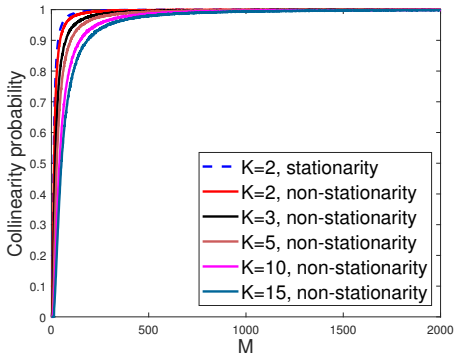

Fig. 6. The probability of collinearity varies with the increase of M under different conditions.

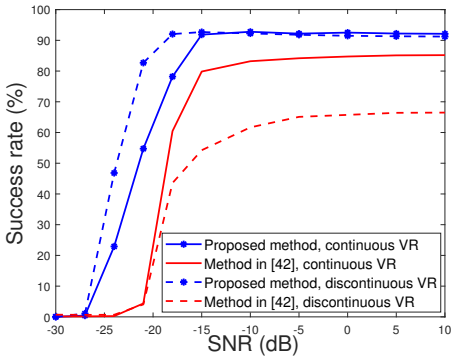

Fig. 7. Success rates comparison in VR estimation methods.

is $\left(0.62\sqrt{D^3/\lambda}, 2D^2/\lambda\right)$, the near-field range is set between 3000λ and 10000λ from the array.

A. Validation of Collinearity Theorem

To validate Theorem 1, three scenarios are considered: spatially stationary and non-stationary cases where $K = 2$, and the non-stationary case where $K > 2$. We increase the array size from 10 to 2000 and carry out $20,000$ Monte Carlo trials, during which the quantity of trials that fulfill the collinearity threshold is tallied. The proportion of the number of trials satisfying the collinearity threshold to the overall number of trials denotes the collinearity probability. In each trial, the VR of each signal is selected randomly, and the position of the signal is also randomly determined within the near-field region of the array. The values of $\left|\frac{c_{2,k'}}{c_{1,k'}}\right|$ in different scenarios are calculated by (28), (31) and (33), respectively. These values are then compared with the collinearity threshold of 0.01. If the value falls below this threshold, it is regarded as collinear. Lastly, the collinearity probabilities at different M values are statistically analyzed, as shown in Fig. 6. It can be observed that for all three scenarios, the probability of collinearity ascends in tandem with augmentation of the value of M, and even when the number of antennas $M = 500$ and the number of sources $K = 15$, the collinearity probability can still exceed 98%. Consequently, it can be deduced that irrespective of the presence or absence of spatial non-stationarity and notwithstanding the variation in the number of signal sources, Theorem 1 invariably holds.

B. Performance of VR Estimation

In Fig. 7, the success rate of the VR estimation method in continuous and discontinuous VR scenarios through $10,000$ Monte Carlo trials is presented, under different SNR values. The SNR is defined as the ratio of the received signal power to the noise variance, where the noise variance is adjusted to reflect the signal attenuation over distance. We set $K = 2$, with angles and ranges randomly selected from the near-field range. For the continuous VR scenario, a segment of subarray is randomly selected from the ELAA as the VR, while for the discontinuous VR scenario, two segments of

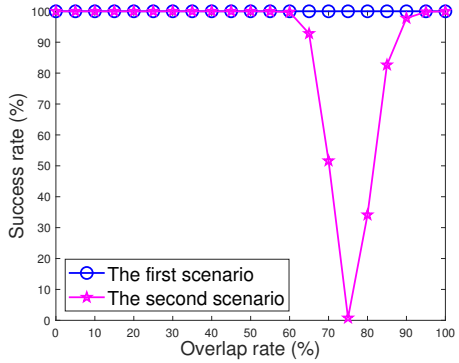

Fig. 8. Success rates of VR estimation in different scenarios.

subarrays are randomly chosen from the ELAA to form the VR. As shown, our proposed method achieves a success rate of over 90% when the SNR is greater than -18 dB in the discontinuous VR scenario; and for the continuous VR scenario, the success rate is over 90% when the SNR exceeds -15 dB. Moreover, the performance of our proposed method is not significantly different between continuous and discontinuous VR scenarios, with VR identified successfully in both cases. Furthermore, compared to the VR identification method in [42], our method achieves a higher overall success rate, especially in discontinuous VR scenarios.

Fig. 8 demonstrates the success rates of our VR estimation method in two specific scenarios. In the first scenario, there is only one signal present, and the VR of this signal gradually expands from a smaller subarray to the entire ELAA, i.e., from spatial non-stationarity to spatial stationarity. Clearly, our method is completely successful in this scenario. In the second scenario, we set the position parameters of two signals to $\{\vartheta_1, r_1\} = \{-30^\circ, 7800\lambda\}$ and $\{\vartheta_2, r_2\} = \{60^\circ, 4500\lambda\}$; additionally, the VRs of two signals are continuous, where one signal's VR is constant, with $\boldsymbol{\phi}_1 = \{101, \cdots, 500\}$, while the other signal's VR is variable, with $\boldsymbol{\phi}_2 = \{1, \cdots, m\}$, with m varying from 100 to 500. As m varies, the overlapping region between $\boldsymbol{\phi}_1$ and $\boldsymbol{\phi}_2$ increases from none to complete coincidence. In this scenario, our method entirely fails when the overlap rate reaches 75%. At this point, through calculation, we find that $\{\frac{p_1 n_1 r_1}{\cos(\vartheta_1)}, \frac{p_2 n_2 r_2}{\cos(\vartheta_2)}\} = \{718.19, 712.98\}$. Due to close proximity of their values, the collinearity theorem thus

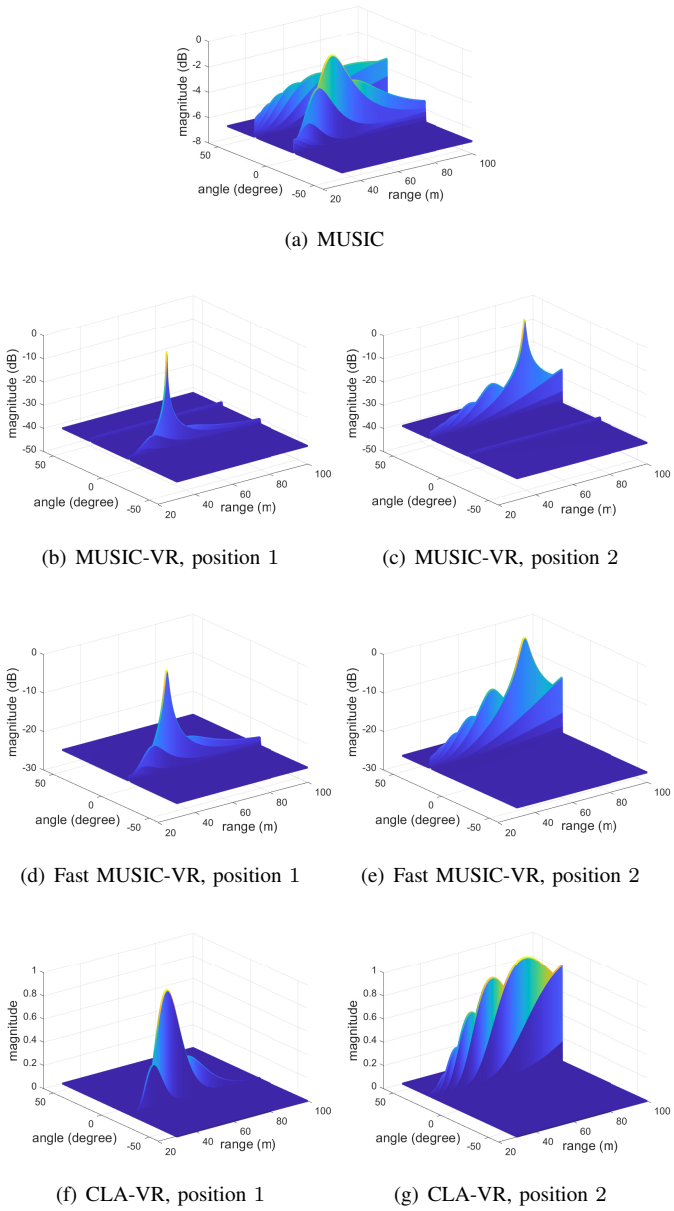

Fig. 9. The spectra of MUSIC, MUSIC-VR, Fast MUSIC-VR, and CLA-VR when the VRs of two signals overlap.

becomes almost invalid.

C. Estimated Spectrum

The performance of our proposed localization algorithms Fast MUSIC-VR and CLA-VR is evaluated by comparing with MUSIC and MUSIC with estimated VR (MUSIC-VR). In MUSIC-VR, we replace the steering vector in the calculated MUSIC spectrum with the steering vector with VR. As described in Subsection III-A, an unknown $\mathbf{\Gamma}$ leads to a mismatch between $\boldsymbol{a}(\tilde{\vartheta},\tilde{r})$ and $\hat{\boldsymbol{a}}(\vartheta_k,r_k)$, resulting in a decrease in accuracy. To solve it, we consider searching in the space using the steering vector with estimated VR. Due to K different VRs, we still need to search K times and the

TABLE I
CPU RUNNING TIME FOR THE FIRST SCENARIO.

Algorithm	Average CPU running time (s)
L1SVD	153.60
L1SVD-VR	185.48
MUSIC	6.52
MUSIC-VR	20.13
Method in [42]	36.06
TSMUSIC	1.83
Fast MUSIC-VR	0.96
CLA-VR	1.90
PSO-VR	8.47

TABLE II
CPU RUNNING TIME FOR THE SECOND SCENARIO.

Algorithm	Average CPU running time (s)
L1SVD	154.01
L1SVD-VR	187.48
MUSIC	6.34
MUSIC-VR	19.23
Method in [42]	33.44
TSMUSIC	1.77
Fast MUSIC-VR	4.40
CLA-VR	1.88
PSO-VR	8.43

spectrum of the k'-th search is given as,

$$S_{k'}(\tilde{\vartheta},\tilde{r}) = \frac{1}{\left(\boldsymbol{a}(\tilde{\vartheta},\tilde{r})\circ\tilde{\boldsymbol{\gamma}}_{k'}\right)^H \boldsymbol{U_N}\boldsymbol{U_N}^H\left(\boldsymbol{a}(\tilde{\vartheta},\tilde{r})\circ\tilde{\boldsymbol{\gamma}}_{k'}\right)}. \tag{16}$$

Then, we can apply MUSIC to covariance matrix for K times with K different spectrum models. The spectrum of CLA-VR is obtained by computing (12), and its magnitude represents the strength of correlation.

In the spectrum estimation experiment, we set $K = 2$, SNR $= 10$ dB, the position of the two signals as $\{\vartheta_1, r_1\} = \{-10°, 5000\lambda\}$ and $\{\vartheta_2, r_2\} = \{30°, 8000\lambda\}$, and the VR information as $\boldsymbol{\phi}_1 = \{1,\cdots,400\}$ and $\boldsymbol{\phi}_2 = \{201,\cdots,500\}$. We estimate the spectrum of the two signals in the overlapping scenario, as depicted in Fig. 9. Notably, the spectrum performance of the MUSIC algorithm is significantly deficient, with not only the primary peak being insufficiently distinct but also pseudo peaks related to one primary peak interfering with the interpretation of another primary peak. In contrast, MUSIC-VR and the proposed methods can successfully identify the two sources.[3] Importantly, our methods differ from the MUSIC algorithm, and the pseudo peaks near one signal's primary peak will not interfere with the judgment of another signal's primary peak. This is because our methods do not simultaneously estimate K sources but instead estimate the spectrum for each source individually, a total of K times. The advantage of this design is that the primary peak of one signal remains unaffected by pseudo peaks from other signals.

[3]The spectrum of the CLA-VR algorithm presented in the figure has undergone a specific processing step, where the values at the grid points of the original spectrum are multiplied by ten to highlight the primary peak.

This article has been accepted for publication in IEEE Transactions on Signal Processing. This is the author's version which has not been fully edited and content may change prior to final publication. Citation information: DOI 10.1109/TSP.2026.3654842

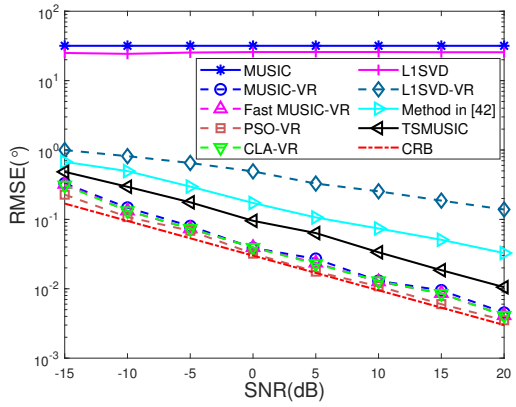

(a) RMSE for angles

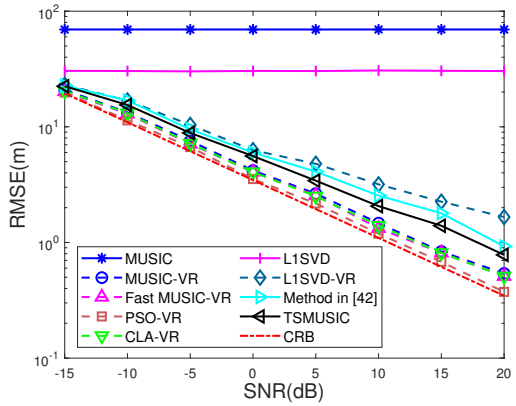

(b) RMSE for ranges

Fig. 10. RMSE comparison of different algorithms for varying SNR, in the scenario where the VRs of three signals are non-overlapping and continuous.

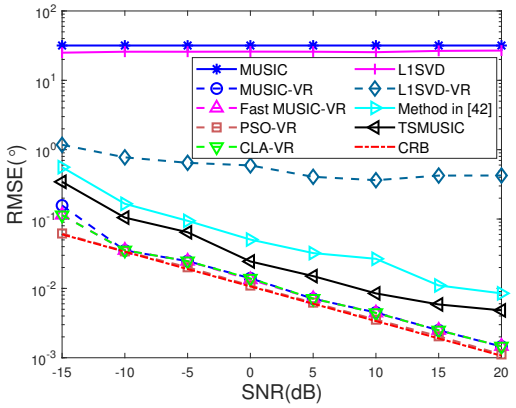

(a) RMSE for angles

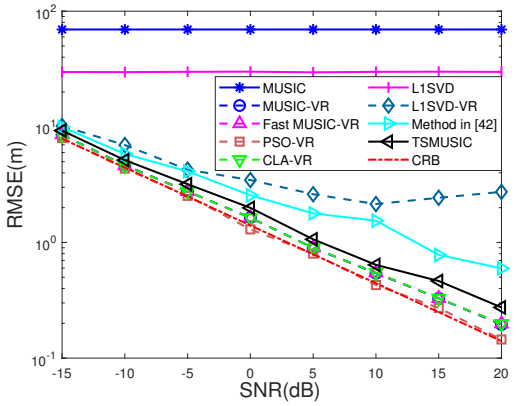

(b) RMSE for ranges

Fig. 11. RMSE comparison of different algorithms for varying SNR, in the scenario where the VRs of only two sources overlap.

D. RMSE

In the root mean square error (RMSE) experiment, we set $K = 3$ and SNR varies from -15 dB to 20 dB. Four scenarios are considered, covering both simple and complex VR scenarios, while maintaining $\{\vartheta_1, r_1\} = \{45°, 6000\lambda\}$, $\{\vartheta_2, r_2\} = \{10°, 7000\lambda\}$ and $\{\vartheta_3, r_3\} = \{-30°, 8000\lambda\}$ unchanged in each scenario. We compare the performance of our three algorithms with MUSIC, MUSIC-VR, L1SVD, L1SVD-VR, the method proposed in [42], and two-stage MUSIC (TSMUSIC).

The first scenario has three non-overlapping signals while the VR of each signal is continuous, i.e., $\boldsymbol{\phi}_1 = \{1, \cdots, 50\}$, $\boldsymbol{\phi}_2 = \{201, \cdots, 250\}$ and $\boldsymbol{\phi}_3 = \{401, \cdots, 450\}$, and the simulation results are shown in Fig. 10. Both in terms of angle estimation and range estimation, it can be observed that the MUSIC algorithm fails due to the presence of pseudo peaks. Similarly, the L1SVD algorithm also fails in this scenario because it cannot effectively utilize the VR information, which leads to model mismatch and ultimately results in estimation errors. However, as the SNR increases, the RMSE of the methods including MUSIC-VR, L1SVD-VR, the method proposed in [42], TSMUSIC and the three algorithms proposed in this paper (i.e., CLA-VR, Fast MUSIC-VR and PSO-VR) shows a significant downward trend. Among these methods, the PSO-VR algorithm performs the best. Its RMSE curve is the closest to the CRB curve. Secondarily, the CLA-VR, Fast MUSIC-VR and MUSIC-VR algorithms achieve good performance, and the remaining three comparative algorithms perform slightly worse, and among them, the L1SVD-VR algorithm has the worst performance.

In order to compare the computing time of each algorithm intuitively, we show the CPU running time for the first scenario in Table I. We can observe that the L1SVD-VR algorithm has the longest running time among all algorithms. By contrast, the MUSIC-VR algorithm has a longer running time than the traditional MUSIC algorithm, which is attributed to its requirement to perform K independent MUSIC operations. Among these comparative algorithms, TSMUSIC algorithm shows a relatively short running time. Among the three algorithms proposed in this paper, Fast MUSIC-VR shows the shortest running time, followed by CLA-VR and then PSO-VR.

The second scenario has two signals overlapping while the third signal does not overlap, i.e., $\boldsymbol{\phi}_1 = \{1, \cdots, 300\}$, $\boldsymbol{\phi}_2 = \{251, \cdots, 400\}$ and $\boldsymbol{\phi}_3 = \{401, \cdots, 500\}$, and the simulation results are shown in Fig. 11. Similar to the first scenario, the MUSIC and L1SVD algorithms still fail. However, as the SNR increases, the RMSE of the other algorithms still shows a significant decreasing trend. Among these methods,

This article has been accepted for publication in IEEE Transactions on Signal Processing. This is the author's version which has not been fully edited and content may change prior to final publication. Citation information: DOI 10.1109/TSP.2026.3654842

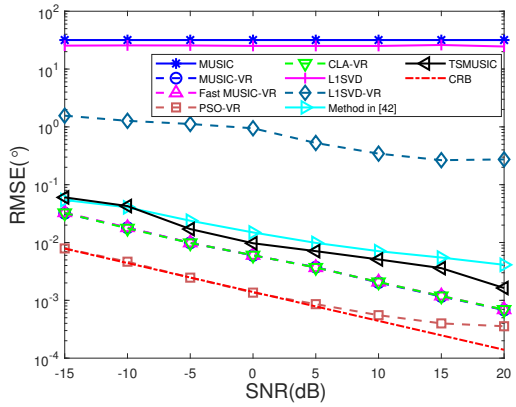

(a) RMSE for angles

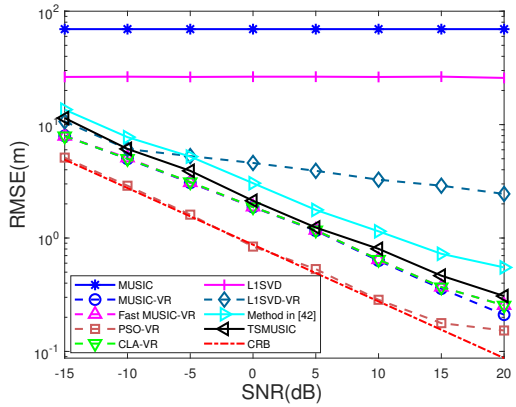

(b) RMSE for ranges

Fig. 12. RMSE comparison of different algorithms for varying SNR, in the scenario where the VRs of three sources overlap and the overlapping region contains at most three sources.

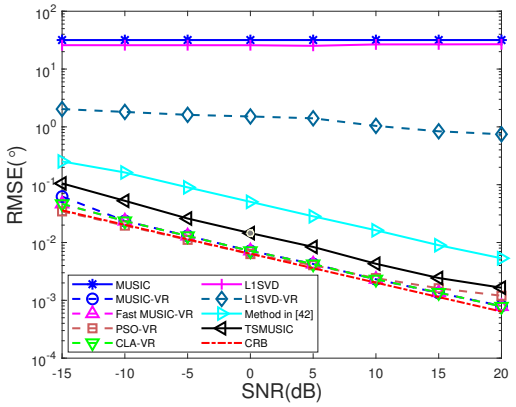

(a) RMSE for angles

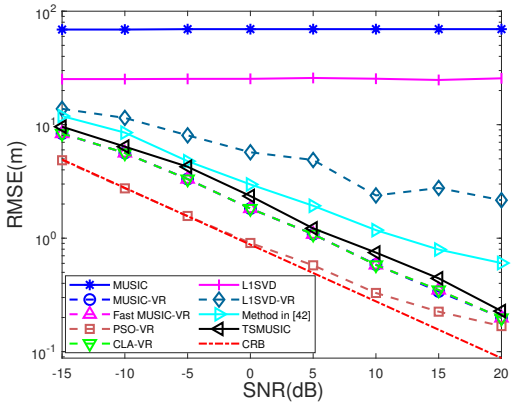

(b) RMSE for ranges

Fig. 13. RMSE comparison of different algorithms for varying SNR, in the scenario where the VR of one source is discontinuous and overlaps with the other two sources.

the PSO-VR algorithm still achieves the best performance, and its RMSE curve almost coincides with the CRB curve. To further compare the computing time of each algorithm, Table II presents the CPU running time for the second scenario. It can be observed that Fast MUSIC-VR's running time increases significantly, while that of other algorithms remains nearly unchanged. This is because Fast MUSIC-VR's running time depends on each VR's array size, which is directly related to the covariance matrix dimension. Specifically, Fast MUSIC-VR runs faster than CLA-VR when each source's VR is relatively small, but CLA-VR achieves shorter average running time for large VRs. Although PSO-VR is not the fastest among the three proposed methods, its inherent gridless nature provides distinct advantages in estimation performance. Thus, each of the proposed methods has its unique advantages.

The third scenario is the mutual overlap of three signal VRs, with three signals present in the overlapping region, i.e., $\boldsymbol{\phi}_1 = \{1, \cdots, 250\}$, $\boldsymbol{\phi}_2 = \{201, \cdots, 300\}$ and $\boldsymbol{\phi}_3 = \{231, \cdots, 400\}$. This scenario represents the most complex case when $K = 3$ and only VR overlaps are considered, and its simulation results are shown in Fig. 12. In this scenario, the coupling between the VRs of the three signals is severe. Therefore, the RMSE curves of algorithms other than MUSIC and L1SVD deviate more significantly from the CRB, particularly in terms of angle estimation. Nevertheless, our proposed algorithms (i.e., CLA-VR, Fast MUSIC-VR, PSO-VR) still remain effective even in this complex scenario, maintaining relatively low RMSE values and ensuring accurate estimation of signal angles and ranges.

The final scenario is a signal with a discontinuous VR, and the VRs of the other two signals overlap with it, but the overlapping regions do not exceed two signals each, i.e., $\boldsymbol{\phi}_1 = \{1, \cdots, 100, 301, \cdots, 400\}$, $\boldsymbol{\phi}_2 = \{71, \cdots, 300\}$ and $\boldsymbol{\phi}_3 = \{381, \cdots, 500\}$, and the results are shown in Fig. 13. We observe that in this scenario, all algorithms except the still ineffective MUSIC and L1SVD achieve successful localization. For the proposed algorithms, their range estimation performance is comparatively poor. Specifically, although their RMSE decreases with increasing SNR, the deviation of range estimation from the CRB is more significant than that in angle estimation. Furthermore, this scenario fully verifies the effectiveness of the proposed algorithms in complex scenarios with discontinuous and overlapping VRs.

In the RMSE experiment with varying number of snapshots, the number of snapshots L is set to vary from 100 to 2000. The angles and ranges of the three sources remain

This article has been accepted for publication in IEEE Transactions on Signal Processing. This is the author's version which has not been fully edited and content may change prior to final publication. Citation information: DOI 10.1109/TSP.2026.3654842

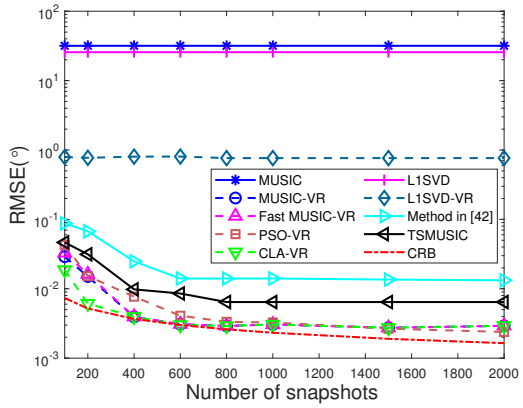

(a) RMSE for angles

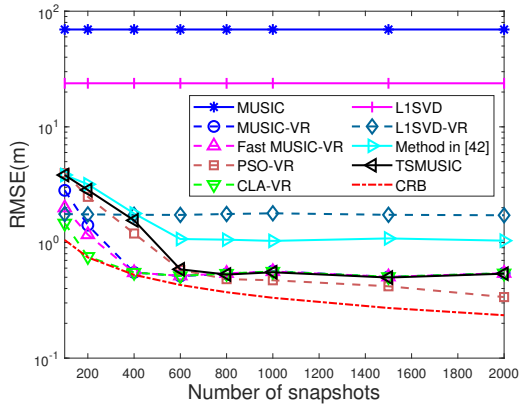

(b) RMSE for ranges

Fig. 14. RMSE comparison of different algorithms for varying L, in the scenario where the VRs of three sources overlap and the overlapping region contains at most two sources.

consistent with those in the previous experiments. The VR is set to $\boldsymbol{\phi}_1 = \{1, \cdots, 250\}$, $\boldsymbol{\phi}_2 = \{221, \cdots, 400\}$ and $\boldsymbol{\phi}_3 = \{371, \cdots, 500\}$, and the SNR is set to 10 dB. Simulation results are presented in Fig. 14, from which it can be seen that the MUSIC and L1SVD algorithms still fail to estimate angles and ranges, while all other comparative algorithms are capable of effective estimation. Additionally, in both angle estimation and range estimation, under the scenario of a small number of snapshots (i.e., $L < 400$), the CLA-VR algorithm demonstrates the best estimation performance compared with other algorithms. Finally, there is a notable performance variation for the PSO-VR algorithm: when $L < 800$, its performance is inferior to that of the CLA-VR, Fast MUSIC-VR, and MUSIC-VR algorithms. However, as the number of snapshots further increases (i.e., $L > 800$), the PSO-VR algorithm gradually exhibits the best performance among these algorithms. This phenomenon is attributed to the gridless nature of the PSO-VR algorithm. This is because the algorithm requires more snapshot data to optimize the particle swarm search and converge to the optimal solution, and it ultimately achieves higher estimation accuracy than the other algorithms once sufficient data is available.

In summary, our three proposed algorithms outperform other comparative methods in ELAA-based source localization, with distinct advantages in balancing accuracy and computational efficiency. Specifically, both CLA-VR and Fast MUSIC-VR achieve localization accuracy comparable to that of MUSIC-VR while exhibiting significantly faster running times. They also demonstrate good localization accuracy when the number of snapshots is small. Furthermore, our PSO-VR algorithm stands out with the highest localization accuracy when the number of snapshots is sufficiently large. Its RMSE curve remains the closest to the CRB even in complex scenarios such as discontinuous or overlapping VR. While its average running time is longer than that of CLA-VR and Fast MUSIC-VR, it is still more computationally efficient than most comparative methods.

VI. Conclusions and Future Work

An exact steering vector model for ELAA has been introduced considering spatial non-stationarity and near-field effects. Building on this model, the collinearity property between the signal subspace eigenvectors and the steering vectors is proved, based on which a VR estimation method is designed. It has a high success rate and remains effective in complex scenarios. Furthermore, three localization algorithms, namely Fast MUSIC-VR, CLA-VR, and PSO-VR, are proposed for angle and range estimation in ELAA. The simplicity of our methods lies in their ability to directly estimate angle and range using the eigenvectors within the signal subspace of the covariance matrix. Numerical results indicate that our methods exhibit a superior RMSE performance and a higher resolution than the comparative algorithms. In the future, we aim to apply the collinearity theorem to more practical scenarios featuring mixed near-field and far-field sources, while expanding its application to uniform planar arrays and a broader range of array configurations. Additionally, the development of deep learning-based methods for related localization tasks will also be a key focus of our future work.

Appendix A
Proof of Theorem 1

According to eigenvalue decomposition, we have,

$$(\boldsymbol{R} - \lambda_{k'}\boldsymbol{I})\boldsymbol{v}_{k'} = \boldsymbol{0}, k' = 1, \cdots, K, \tag{17}$$

with $\boldsymbol{R} = \hat{\boldsymbol{A}}\boldsymbol{P}\hat{\boldsymbol{A}}^H + \sigma^2\boldsymbol{I}$, where σ^2 is the noise power, and $\boldsymbol{P} = diag(p_1, \cdots, p_K)$ denotes signal power. According to subspace theory, we have,

$$\boldsymbol{v}_{k'} = c_{1,k'}\hat{\boldsymbol{a}}(\vartheta_1, r_1) + \cdots + c_{K,k'}\hat{\boldsymbol{a}}(\vartheta_K, r_K), \tag{18}$$

where $c_{1,k'}, \cdots, c_{K,k'}$ are complex coefficients. To find the relationship between the steering vector $\{\hat{\boldsymbol{a}}(\vartheta_k, r_k)\}_{k=1}^K$ and $\boldsymbol{v}_{k'}$, we can find the ratio between the coefficients $\{c_{k,k'}\}_{k=1}^K$. For example, if $c_{1,k'}$ is much greater than other coefficients, we can say $\hat{\boldsymbol{a}}(\vartheta_1, r_1)$ and $\boldsymbol{v}_{k'}$ are collinear. Then, substituting (18) into (17), we can obtain the following M equations,

$$\sum_{k=1}^{K} \omega(m,k)c_{k,k'} = 0; \quad m = 1, \cdots, M, \tag{19}$$

with $\omega(m,k) = (\sigma^2 + \psi_k - \lambda_{k'})\hat{\boldsymbol{A}}_{(m,k)} + g(m,k)$, where $\hat{\boldsymbol{A}}_{(m,k)}$ is the (m,k)-th element of $\hat{\boldsymbol{A}}$, ψ_k is the total power of the k-th signals received by ELAA, given as,

$$\psi_k = p_k \|\hat{\boldsymbol{a}}(\vartheta_k, r_k)\|_2^2, \tag{20}$$

and $g(m,k)$ denotes the correlation between the steering vector of the k-th signal and the steering vectors of others, given by,

$$\begin{aligned} g(m,k) =& p_1 \left[\hat{\boldsymbol{a}}^H(\vartheta_1, r_1)\hat{\boldsymbol{a}}(\vartheta_k, r_k)\right] \hat{\boldsymbol{A}}_{(m,1)} + \cdots \\ &+ p_{k-1} \left[\hat{\boldsymbol{a}}^H(\vartheta_{k-1}, r_{k-1})\hat{\boldsymbol{a}}(\vartheta_k, r_k)\right] \hat{\boldsymbol{A}}_{(m,k-1)} \\ &+ p_{k+1} \left[\hat{\boldsymbol{a}}^H(\vartheta_{k+1}, r_{k+1})\hat{\boldsymbol{a}}(\vartheta_k, r_k)\right] \hat{\boldsymbol{A}}_{(m,k+1)} + \cdots \\ &+ p_K \left[\hat{\boldsymbol{a}}^H(\vartheta_K, r_K)\hat{\boldsymbol{a}}(\vartheta_k, r_k)\right] \hat{\boldsymbol{A}}_{(m,K)}. \end{aligned} \tag{21}$$

Since $M>K$, we only need to solve $K-1$ equations in (19) to obtain the ratio between each pair of coefficients, e.g., $\left|\frac{c_{2,k'}}{c_{1,k'}}\right|, \left|\frac{c_{3,k'}}{c_{1,k'}}\right|, \cdots, \left|\frac{c_{K,k'}}{c_{1,k'}}\right|$. In the following, we first consider the case of $K=2$, and then extend it to the case of $K>2$.

A. The Case of $K = 2$

From (19), we have $\omega(m,1)c_{1,k'} + \omega(m,2)c_{2,k'} = 0$. Then, the ratio $\left|\frac{c_{2,k'}}{c_{1,k'}}\right|$ is given as,

$$\begin{aligned} \left|\frac{c_{2,k'}}{c_{1,k'}}\right| &= \left|\frac{\omega(m,1)}{\omega(m,2)}\right| \\ &= \left|\frac{\left[\sigma^2 + \psi_1 - \lambda_{k'}\right] \hat{\boldsymbol{A}}_{(m,1)} + g(m,1)}{\left[\sigma^2 + \psi_2 - \lambda_{k'}\right] \hat{\boldsymbol{A}}_{(m,2)} + g(m,2)}\right|. \end{aligned} \tag{22}$$

According to [46], as $M \to \infty$, the eigenvalues $\lambda_{k'} = \psi_k + \sigma^2$. In this case, we can see that there are two possibilities, i.e., $\lambda_{k'} = \psi_1 + \sigma^2$ or $\lambda_{k'} = \psi_2 + \sigma^2$. Without loss of generality, we assume that $\lambda_{k'} = \psi_1 + \sigma^2$, and then consider the scenarios of both spatial stationarity and spatial non-stationarity.

1) Spatial Stationarity: When $\lambda_{k'} = \psi_1 + \sigma^2$, (22) is modified as,

$$\left|\frac{c_{2,k'}}{c_{1,k'}}\right| = \left|\frac{g(m,1)}{(\psi_2 - \psi_1)\hat{\boldsymbol{A}}_{(m,2)} + g(m,2)}\right|. \tag{23}$$

In the case of spatial stationarity, (20) is given as,

$$\psi_k = p_k \left[\left(\frac{r_k}{r_{1,k}}\right)^2 + \cdots + \left(\frac{r_k}{r_{M,k}}\right)^2\right]. \tag{24}$$

By defining the function,

$$\begin{aligned} f(m) &= \left(\frac{r_k}{r_{m,k}}\right)^2 \\ &= \frac{r_k^2}{(md - r_k \sin(\vartheta_k))^2 + (r_k \cos(\vartheta_k))^2}, \end{aligned} \tag{25}$$

(24) can be rewritten as,

$$\psi_k = p_k \left[f\left(-\frac{M-1}{2}\right) + \cdots + f\left(\frac{M-1}{2}\right)\right]. \tag{26}$$

Obviously, (25) is symmetric about $m = \frac{r_k sin(\vartheta_k)}{d}$, and thus, we only focus on $\frac{1}{2}\psi_k = p_k \left[f\left(\frac{r_k \sin(\vartheta_k)}{d}\right) + \cdots + f\left(\frac{M-1}{2}\right)\right]$. In Fig. 15, The bar chart depicts the discrete values of $f(m)$ at various points, and the total area of the bar chart represents the summation of these discrete values of $f(m)$. Meanwhile, the area under the curve $f(m)$ signifies the definite integral of $f(m)$ within the corresponding range. It is observed that the area covered by the bar chart exceeds the area beneath the curve in Fig. 15(a), but falls short of that in Fig. 15(b), i.e.,

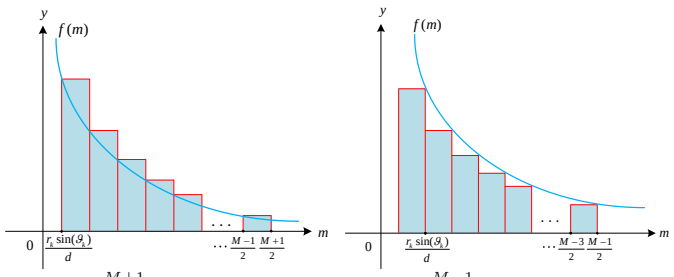

Fig. 15. Transform the summation of a sequence into a definite integral.

$$p_k \int_{\frac{r_k \sin(\vartheta_k)}{d}}^{\frac{M+1}{2}} f(m)dm \le \frac{1}{2}\psi_k \le p_k \int_{\frac{r_k \sin(\vartheta_k)}{d}-1}^{\frac{M-1}{2}} f(m)dm, \tag{27}$$

Define $A = \frac{\pi p_k r_k}{\lambda \cos(\vartheta_k)}$ and $B = \frac{2p_k r_k}{\lambda \cos(\vartheta_k)} \arctan\left(\frac{d}{r_k \cos(\vartheta_k)}\right)$. When $M \to \infty$, we have $p_k \int_{\frac{r_k \sin(\vartheta_k)}{d}}^{\frac{M+1}{2}} f(m)dm = A$ and $p_k \int_{\frac{r_k \sin(\vartheta_k)}{d}-1}^{\frac{M-1}{2}} f(m)dm = A+B$. Since the range of the near-field region is $\left(0.62\sqrt{D^3/\lambda}, 2D^2/\lambda\right)$, where $D = (M-1)d$ is the array aperture [47], when $M \to \infty$, r_k could be infinity. Therefore, when $A \to \infty$, $B = \frac{2p_k d}{\lambda \cos^2(\vartheta_k)}$ which is a constant,[4] and A is significantly greater than B. Furthermore, as $A \le \frac{1}{2}\psi_k \le A + B$, it is possible to derive $\frac{1}{2}\psi_k \to A$ by applying the squeeze theorem. Thus, we conclude that $\psi_k = 2A = \frac{2\pi p_k r_k}{\lambda \cos(\vartheta_k)}$, so $\psi_2 - \psi_1 = \frac{2\pi}{\lambda}\left(\frac{p_2 r_2}{\cos(\vartheta_2)} - \frac{p_1 r_1}{\cos(\vartheta_1)}\right)$, and then (23) can be rewritten as,

$$\left|\frac{c_{2,k'}}{c_{1,k'}}\right| = \left|\frac{g(m,1)}{\left[\frac{2\pi}{\lambda}\left(\frac{p_2 r_2}{\cos(\vartheta_2)} - \frac{p_1 r_1}{\cos(\vartheta_1)}\right)\right] \hat{\boldsymbol{A}}_{(m,2)} + g(m,2)}\right|. \tag{28}$$

When $M \to \infty$, the correlation between different steering vectors can be ignored, i.e., $g(m,1) \to 0$ and $g(m,2) \to 0$, and $\hat{\boldsymbol{A}}_{(m,2)}$ is a complex number with a non-zero modulus. Consequently, we can observe that the determining factor in (28) is $\frac{2\pi}{\lambda}\left(\frac{p_2 r_2}{\cos(\vartheta_2)} - \frac{p_1 r_1}{\cos(\vartheta_1)}\right)$. When $\frac{p_2 r_2}{\cos(\vartheta_2)} \neq \frac{p_1 r_1}{\cos(\vartheta_1)}$, it is a non-zero value, and it becomes larger as $\left|\frac{p_2 r_2}{\cos(\vartheta_2)} - \frac{p_1 r_1}{\cos(\vartheta_1)}\right|$ increases. Therefore, we can deduce through analysis that $\left|\frac{c_{2,k'}}{c_{1,k'}}\right| \to 0$ when $\frac{p_2 r_2}{\cos(\vartheta_2)} \neq \frac{p_1 r_1}{\cos(\vartheta_1)}$. Consequently, the proportion of steering vector $\hat{\boldsymbol{a}}(\vartheta_1, r_1)$ on the k'-th eigenvector $\boldsymbol{v}_{k'}$ is much greater than that of steering vector $\hat{\boldsymbol{a}}(\vartheta_2, r_2)$, which means that $\boldsymbol{v}_{k'}$ and $\hat{\boldsymbol{a}}(\vartheta_1, r_1)$ are collinear. Similarly,

[4]We do not consider signals parallel to the array direction, i.e., $\vartheta_k \in (-90°, 90°)$.

$$\left|\frac{c_{i,k'}}{c_{j,k'}}\right| = \left|\frac{\varpi_j}{\varpi_i + \frac{2\pi}{\lambda}\left(\frac{p_i n_i r_i}{\cos(\vartheta_i)} - \frac{p_j n_j r_j}{\cos(\vartheta_j)}\right)\left(q_1^K \hat{\boldsymbol{A}}_{(m_1,i)} + \cdots + q_{K-1}^K \hat{\boldsymbol{A}}_{(m_{K-1},i)}\right)}\right|. \tag{33}$$

$$\left|\frac{c_{i,k'}}{c_{j,k'}}\right| = \left|\frac{\varpi_j}{\varpi_i + M\left(p_i n_i - p_j n_j\right)\left(q_1^K \hat{\boldsymbol{A}}_{(m_1,i)} + \cdots + q_{K-1}^K \hat{\boldsymbol{A}}_{(m_{K-1},i)}\right)}\right|. \tag{36}$$

the other eigenvector is collinear with the steering vector $\hat{\boldsymbol{a}}(\vartheta_2, r_2)$.

2) Spatial Non-Stationarity: When the VRs of two signals do not overlap, i.e., $\boldsymbol{\phi}_1 \cap \boldsymbol{\phi}_2 = \emptyset$, it is known that $g(m,1) = g(m,2) = 0$. When $m \in \boldsymbol{\phi}_1$, (19) can be simplified as,

$$\left(\sigma^2 + \psi_1 - \lambda_{k'}\right)\hat{\boldsymbol{A}}_{(m,1)} c_{1,k'} = 0. \tag{29}$$

Since $\sigma^2 + \psi_1 - \lambda_{k'} = 0$, from (29) we know $c_{1,k'}$ is non-zero-valued. Additionally, when $m \in \boldsymbol{\phi}_2$, (19) can be simplified as,

$$(\psi_2 - \psi_1)\hat{\boldsymbol{A}}_{(m,2)} c_{2,k'} = 0. \tag{30}$$

Since $\psi_1 \neq \psi_2$, we have $c_{2,k'} = 0$. From (18), we can conclude that $\boldsymbol{v}_{k'} = c_{1,k'}\hat{\boldsymbol{a}}(\vartheta_1, r_1)$. Similarly, the other eigenvector equals $c_{2,k'}\hat{\boldsymbol{a}}(\vartheta_2, r_2)$. As a result, we can conclude that $\{\boldsymbol{v}_1, \boldsymbol{v}_2\}$ are collinear with $\{\hat{\boldsymbol{a}}(\vartheta_1, r_1), \hat{\boldsymbol{a}}(\vartheta_2, r_2)\}$.

When the VRs of two signals overlap, i.e., $\boldsymbol{\phi}_1 \cap \boldsymbol{\phi}_2 \neq \emptyset$, we can not ignore the impact of $g(m,k)$, and then, (22) can be rewritten as,

$$\left|\frac{c_{2,k'}}{c_{1,k'}}\right| = \left|\frac{g(m,1)}{\left[\frac{2\pi}{\lambda}\left(\frac{p_2 n_2 r_2}{\cos(\vartheta_2)} - \frac{p_1 n_1 r_1}{\cos(\vartheta_1)}\right)\right]\hat{\boldsymbol{A}}_{(m,2)} + g(m,2)}\right|, \tag{31}$$

where $n_1, n_2 \in (0,1]$ represent the adjustment coefficients of VR, expressed as $n_1 = \frac{\|\hat{\boldsymbol{a}}(\vartheta_1,r_1)\|_2^2}{\|\boldsymbol{a}(\vartheta_1,r_1)\|_2^2}$ and $n_2 = \frac{\|\hat{\boldsymbol{a}}(\vartheta_2,r_2)\|_2^2}{\|\boldsymbol{a}(\vartheta_2,r_2)\|_2^2}$. $g(m,1)$ and $g(m,2)$ are unpredictable terms, but according to their definitions, when $M \to \infty$, we can infer that their values are very small, i.e, $g(m,1) \to 0$ and $g(m,2) \to 0$. Moreover, $\hat{\boldsymbol{A}}_{(m,2)}$ is also a complex number with a non-zero modulus. Therefore, as long as $\frac{p_2 n_2 r_2}{\cos(\vartheta_2)} \neq \frac{p_1 n_1 r_1}{\cos(\vartheta_1)}$, $\left|\frac{c_{2,k'}}{c_{1,k'}}\right| \to 0$ can be derived. As a result, $\{v_1, v_2\}$ and $\{\hat{\boldsymbol{a}}(\vartheta_1, r_1), \hat{\boldsymbol{a}}(\vartheta_2, r_2)\}$ also have collinear relationship in this situation.

B. The Case of K>2

Now we discuss the case of K>2. From (19), we randomly select $K-1$ equations. By solving these equations, we have,

$$\left|\frac{c_{i,k'}}{c_{j,k'}}\right| = \left|\frac{q_1^K \omega(m_1,j) + \cdots + q_{K-1}^K \omega(m_{K-1},j)}{q_1^K \omega(m_1,i) + \cdots + q_{K-1}^K \omega(m_{K-1},i)}\right|, \tag{32}$$

where $q_r^K = (-1)^{r-1}\frac{(K-2)!}{(r-1)!(K-r-1)!}$, $r = 1, \cdots, K-1$ are real coefficients, and $r!$ denotes the factorial of r, by deducing that they satisfy $q_1^K + \cdots + q_{K-1}^K = 0$. These coefficients are essentially the deformation of Pascal's Triangle, and it can be derived through the relevant knowledge of Pascal's Triangle [48]. Similar to the case of $K = 2$, we assume that $\lambda_{k'} = \psi_j + \sigma^2$, and substituting $\omega(m,k) = (\sigma^2 + \psi_k - \lambda_{k'})\hat{\boldsymbol{A}}_{(m,k)} + g(m,k)$ into (32), we can derive (33) when spatial non-stationarity is considered where $\varpi_i = q_1^K g(m_1,i) + \cdots + q_{K-1}^K g(m_{K-1},i)$ and $\varpi_j = q_1^K g(m_1,j) + \cdots + q_{K-1}^K g(m_{K-1},j)$. Without loss of generality, we consider that $K = 3$ and there exist overlapping regions between VRs. Under this scenario, $q_1^3 = 1, q_2^3 = -1$ and (33) becomes,

$$\left|\frac{c_{i,k'}}{c_{j,k'}}\right| = \left|\frac{\varpi_j}{\varpi_i + \frac{2\pi}{\lambda}\left(\frac{p_i n_i r_i}{\cos(\vartheta_i)} - \frac{p_j n_j r_j}{\cos(\vartheta_j)}\right)\left(\hat{\boldsymbol{A}}_{(m_1,i)} - \hat{\boldsymbol{A}}_{(m_2,i)}\right)}\right|. \tag{34}$$

When $M \to \infty$, we can disregard the minor impact of the correlation between the steering vectors of K signals, i.e., $\varpi_i \to 0$ and $\varpi_j \to 0$. However, as K increases, $q_1^K \hat{\boldsymbol{A}}_{(m_1,i)} + \cdots + q_{K-1}^K \hat{\boldsymbol{A}}_{(m_{K-1},i)}$ in (33) will become increasingly complex, leading to an increased probability of non-collinear scenarios occurring. Nevertheless, when $\frac{p_i n_i r_i}{\cos(\vartheta_i)} \neq \frac{p_j n_j r_j}{\cos(\vartheta_j)}$, there is a high probability that $\left|\frac{c_{i,k'}}{c_{j,k'}}\right| \to 0$. To summarize, the eigenvectors $\{\boldsymbol{v}_1, \cdots, \boldsymbol{v}_K\}$ and the steering vectors $\{\hat{\boldsymbol{a}}(\vartheta_1, r_1), \cdots, \hat{\boldsymbol{a}}(\vartheta_K, r_K)\}$ are collinear in most cases.

For the near-field model based on the Fresnel approximation and the far-field model, the amplitude has no variation, which remains constant at one. Therefore, (20) can be rewritten as:

$$\psi_k = p_k M. \tag{35}$$

Subsequently, (33) can be reformulated as (36). Thus, as $M \to \infty$, if $p_i n_i \neq p_j n_j$, there is a high probability that $\left|\frac{c_{i,k'}}{c_{j,k'}}\right| \to 0$. In this case, it is highly likely that the steering vectors and eigenvectors in this model also have a collinear relationship. On the other hand, if $p_i n_i = p_j n_j$, the value of $\left|\frac{c_{i,k'}}{c_{j,k'}}\right|$ mainly fluctuates around 1 and does not change with the increase of M, which indicates that there is no collinear relationship between the steering vectors and the eigenvectors.

REFERENCES

[1] M. Cui and L. Dai, "Channel estimation for extremely large-scale MIMO: Far-field or near-field?" *IEEE Trans. Commun.*, vol. 70, no. 4, pp. 2663–2677, 2022.

[2] A. Amiri, S. Rezaie, C. N. Manchón, and E. De Carvalho, "Distributed receiver processing for extra-large MIMO arrays: A message passing approach," *IEEE Trans. Wireless Commun.*, vol. 21, no. 4, pp. 2654–2667, 2021.

[3] X. Yang, F. Cao, M. Matthaiou, and S. Jin, "On the uplink transmission of extra-large scale massive MIMO systems," *IEEE Trans. Veh. Technol.*, vol. 69, no. 12, pp. 15 229–15 243, 2020.

[4] X. Wei and L. Dai, "Channel estimation for extremely large-scale massive MIMO: Far-field, near-field, or hybrid-field?" *IEEE Commun. Lett.*, vol. 26, no. 1, pp. 177–181, 2021.

[5] H. Iimori, T. Takahashi, K. Ishibashi, G. T. F. de Abreu, D. González, and O. Gonsa, "Joint activity and channel estimation for extra-large MIMO systems," *IEEE Trans. Wireless Commun.*, vol. 21, no. 9, pp. 7253–7270, 2022.

[6] Z. Dong and Y. Zeng, "Near-field spatial correlation for extremely large-scale array communications," *IEEE Commun. Lett.*, vol. 26, no. 7, pp. 1534–1538, 2022.

[7] H. Lu and Y. Zeng, "Near-field modeling and performance analysis for multi-user extremely large-scale MIMO communication," *IEEE Commun. Lett.*, vol. 26, no. 2, pp. 277–281, 2021.

[8] E. De Carvalho, A. Ali, A. Amiri, M. Angjelichinoski, and R. W. Heath, "Non-stationarities in extra-large-scale massive MIMO," *IEEE Wireless Commun.*, vol. 27, no. 4, pp. 74–80, 2020.

[9] J. He, T. Shu, L. Li, and T.-K. Truong, "Mixed near-field and far-field localization and array calibration with partly calibrated arrays," *IEEE Trans. Signal Process.*, vol. 70, pp. 2105–2118, 2022.

[10] L. Bai, Z. Huang, X. Zhang, and X. Cheng, "A non-stationary 3D model for 6G massive MIMO mmWave UAV channels," *IEEE Trans. Wireless Commun.*, vol. 21, no. 6, pp. 4325–4339, 2021.

[11] Y. Su, X. Wang, and X. Lan, "Co-prime array interpolation for DOA estimation using deep matrix iterative network," *IEEE Trans. Instrum. Meas.*, vol. 73, pp. 1–12, 2024.

[12] W. Wang, X. Wang, Y. Guo, and G. Gui, "Parameter estimation with bistatic MIMO radar: A coarray tensor decomposition framework," *IEEE Trans. Aerosp. Electron. Syst.*, pp. 1–16, 2024.

[13] D. Dardari, N. Decarli, A. Guerra, and F. Guidi, "LOS/NLOS near-field localization with a large reconfigurable intelligent surface," *IEEE Trans. Wireless Commun.*, vol. 21, no. 6, pp. 4282–4294, 2022.

[14] F. Guidi and D. Dardari, "Radio positioning with EM processing of the spherical wavefront," *IEEE Trans. Wireless Commun.*, vol. 20, no. 6, pp. 3571–3586, 2021.

[15] Q. Yang, A. Guerra, F. Guidi, N. Shlezinger, H. Zhang, D. Dardari, B. Wang, and Y. C. Eldar, "Near-field localization with dynamic metasurface antennas," *IEEE Int. Conf. Acoust., Speech, Signal Process. (ICASSP)*, pp. 1–5, 2023.

[16] W. Zuo, J. Xin, W. Liu, N. Zheng, H. Ohmori, and A. Sano, "Localization of near-field sources based on linear prediction and oblique projection operator," *IEEE Trans. Signal Process.*, vol. 67, no. 2, pp. 415–430, 2019.

[17] C. Cheng, S. Liu, H. Wu, and Y. Zhang, "An efficient maximum-likelihood-like algorithm for near-field coherent source localization," *IEEE Transa. Antennas Propag.*, vol. 70, no. 7, pp. 6111–6116, 2022.

[18] X. Wu and W.-P. Zhu, "Single far-field or near-field source localization with sparse or uniform cross array," *IEEE Trans. Veh. Technol.*, vol. 69, no. 8, pp. 9135–9139, 2020.

[19] A. M. Molaei, B. Zakeri, and S. M. Hosseini Andargoli, "Components separation algorithm for localization and classification of mixed near-field and far-field sources in multipath propagation," *IEEE Trans. Signal Process.*, vol. 68, pp. 404–419, 2020.

[20] Z. Zheng, M. Fu, W.-Q. Wang, S. Zhang, and Y. Liao, "Localization of mixed near-field and far-field sources using symmetric double-nested arrays," *IEEE Trans. Antennas Propag.*, vol. 67, no. 11, pp. 7059–7070, 2019.

[21] X. Wu, "Localization of far-field and near-field signals with mixed sparse approach: A generalized symmetric arrays perspective," *Signal Process.*, vol. 175, p. 107665, 2020.

[22] J. Fang, H. Chen, W. Liu, S. Yang, C. Yuen, and H. C. So, "Three-dimensional localization of mixed near-field and far-field sources based on a unified exact propagation model," *IEEE Trans. Signal Process.*, vol. 73, pp. 245–258, 2025.

[23] A. Elzanaty, J. Liu, A. Guerra, F. Guidi, Y. Ma, and R. Tafazolli, "Near and far field model mismatch: Implications on 6G communications, localization, and sensing," *IEEE Internet Things Mag.*, vol. 7, no. 5, pp. 120–126, 2024.

[24] H. Chen, A. Elzanaty, R. Ghazalian, M. F. Keskin, R. Jäntti, and H. Wymeersch, "Channel model mismatch analysis for XL-MIMO systems from a localization perspective," in *Proc. IEEE Glob. Commun. Conf.*, 2022, pp. 1588–1593.

[25] B. Friedlander, "Localization of signals in the near-field of an antenna array," *IEEE Trans. Signal Process.*, vol. 67, no. 15, pp. 3885–3893, 2019.

[26] T. Shu, J. He, and L. Li, "Near-field passive localization and gain-phase compensation with partly calibrated arrays," *IEEE Trans. Aerosp. Electron. Syst.*, vol. 58, no. 1, pp. 712–719, 2022.

[27] J. He, L. Li, T. Shu, and T.-K. Truong, "Mixed near-field and far-field source localization based on exact spatial propagation geometry," *IEEE Trans. Veh. Technol.*, vol. 70, no. 4, pp. 3540–3551, 2021.

[28] A. Dell'Aversano, A. Cuccaro, M. A. Maisto, R. Scapaticci, G. Leone, and R. Solimene, "Near-field MUSIC algorithm for target localization," *IEEE Antennas Wireless Propag. Lett.*, vol. 24, no. 6, pp. 1357–1361, 2025.

[29] A. Elzanaty, A. Guerra, F. Guidi, and M.-S. Alouini, "Reconfigurable intelligent surfaces for localization: Position and orientation error bounds," *IEEE Trans. Signal Process.*, vol. 69, pp. 5386–5402, 2021.

[30] Z. Wang, P. Ramezani, Y. Liu, and E. Björnson, "Near-field localization and sensing with large-aperture arrays: From signal modeling to processing," *IEEE Signal Process. Mag.*, vol. 42, no. 1, pp. 74–87, 2025.

[31] Z. Yuan, J. Zhang, Y. Ji, G. F. Pedersen, and W. Fan, "Spatial non-stationary near-field channel modeling and validation for massive MIMO systems," *IEEE Trans. Antennas Propag.*, vol. 71, no. 1, pp. 921–933, 2023.

[32] Y. Chen and L. Dai, "Non-stationary channel estimation for extremely large-scale MIMO," *IEEE Trans. Wireless Commun.*, vol. 23, no. 7, pp. 7683–7697, 2024.

[33] S. Hou, Y. Wang, T. Zeng, and S. Wu, "Sparse channel estimation for spatial non-stationary massive MIMO channels," *IEEE Commu. Lett.*, vol. 24, no. 3, pp. 681–684, 2019.

[34] J. C. Marinello Filho, G. Brante, R. D. Souza, and T. Abrão, "Exploring the non-overlapping visibility regions in XL-MIMO random access and scheduling," *IEEE Trans. Wireless Commun.*, vol. 21, no. 8, pp. 6597–6610, 2022.

[35] O. S. Nishimura, J. C. Marinello, and T. Abrão, "A grant-based random access protocol in extra-large massive MIMO system," *IEEE Commun. Lett.*, vol. 24, no. 11, pp. 2478–2482, 2020.

[36] Y. Han, M. Li, S. Jin, C.-K. Wen, and X. Ma, "Deep learning-based FDD non-stationary massive MIMO downlink channel reconstruction," *IEEE J. Sel. Areas Commun.*, vol. 38, no. 9, pp. 1980–1993, 2020.

[37] L. Qiao, A. Liao, Z. Li, H. Wang, Z. Gao, X. Gao, Y. Su, P. Xiao, L. You, and D. W. K. Ng, "Sensing user's activity, channel, and location with near-field extra-large-scale MIMO," *IEEE Trans. Commun.*, vol. 72, no. 2, pp. 890–906, 2024.

[38] J. N. Pisharody, A. Rajoriya, and R. Budhiraja, "Near-field channel estimation for XL-MIMO systems using variational Bayesian learning," *IEEE Trans. Wireless Commun.*, pp. 1–1, 2024.

[39] K. Zhi, C. Pan, H. Ren, K. K. Chai, C.-X. Wang, R. Schober, and X. You, "Performance analysis and low-complexity design for XL-MIMO with near-field spatial non-stationarities," *IEEE J. Sel. Areas Commun.*, vol. 42, no. 6, pp. 1656–1672, 2024.

[40] D. Liu, J. Wang, Y. Li, Y. Han, R. Ding, J. Zhang, S. Jin, and T. Q. Quek, "Location-based visible region recognition in extra-large massive MIMO systems," *IEEE Trans. Veh. Technol.*, vol. 72, no. 6, pp. 8186–8191, 2023.

[41] Y. Han, S. Jin, C.-K. Wen, and T. Q. S. Quek, "Localization and channel reconstruction for extra large RIS-assisted massive MIMO systems," *IEEE J. Sel. Topics Signal Process.*, vol. 16, no. 5, pp. 1011–1025, 2022.

[42] J. Tian, Y. Han, S. Jin, and M. Matthaiou, "Low-overhead localization and VR identification for subarray-based ELAA systems," *IEEE Wireless Commun. Lett.*, vol. 12, no. 5, pp. 784–788, 2023.

[43] X. Wu, J. Sun, X. Jia, and S. Wang, "Source localization for extremely large-scale antenna arrays with spatial non-stationarity," *IEEE Int. Conf. Acoust., Speech, Signal Process. (ICASSP)*, pp. 1–5, 2023.

[44] R. Eberhart and J. Kennedy, "A new optimizer using particle swarm theory," in *MHS95. Proc. 6th Int. Symp. Micro Mach. Hum. Sci.*, 1995, pp. 39–43.

[45] D. Wang, D. Tan, and L. Liu, "Particle swarm optimization algorithm: an overview," *Soft Comput.*, vol. 22, pp. 387–408, 2018.

[46] J. B. Andersen, "Array gain and capacity for known random channels with multiple element arrays at both ends," *IEEE J. Sel. Areas Commun.*, vol. 18, no. 11, pp. 2172–2178, 2000.

[47] H. Lu, Y. Zeng, C. You, Y. Han, J. Zhang, Z. Wang, Z. Dong, S. Jin, C.-X. Wang, T. Jiang, X. You, and R. Zhang, "A tutorial on near-field XL-MIMO communications towards 6G," *IEEE Commun. Surveys Tuts.*, pp. 1–1, 2024.

[48] K. H. Rosen, *Discrete Mathematics and Its Applications*, 7th ed. McGraw-Hill, 2012.

This article has been accepted for publication in IEEE Transactions on Signal Processing. This is the author's version which has not been fully edited and content may change prior to final publication. Citation information: DOI 10.1109/TSP.2026.3654842

Xiaohuan Wu (M'16) received the B.S. and Ph.D. degrees from the College of Telecommunication and Information Engineering, Nanjing University of Posts and Telecommunications, Nanjing, China, in 2010 and 2017, respectively, where he is currently an Associate Professor. He has published more than 50 journal and conference papers. His current research interests include array signal processing, compressive sensing, wireless communications and deep learning. He is an associate editor for the Journal of the Franklin Institute.

Jin Qiu received the B.S. degree in communication engineering from Changsha University of Science and Technology, Changsha, China, in 2023. He is currently pursuing the M.S. degree in signal and information processing with Nanjing University of Posts and Telecommunications, Nanjing, China. His research interests include extremely large-scale antenna array and source localization.

Ji Sun received the B.S. degree in Electronic and Information Engineering from Nantong University, Nantong, China, in 2021, and the M.S. degree in Electronic Information from Nanjing University of Posts and Telecommunications, Nanjing, China, in 2024. His research interests include extremely large-scale antenna array and source localization.

Wei Liu (S'01-M'04-SM'10) received his BSc (Space Physics) and LLB (Intellectual Property Law) degrees from Peking University, China, in 1996 and 1997, respectively, MPhil from the Department of Electrical and Electronic Engineering, University of Hong Kong in 2001, and PhD from the School of Electronics and Computer Science, University of Southampton, UK, in 2003. He then worked as a postdoc first at Southampton and later at Imperial College London. From 2005 to 2023, he was a Lecturer/Senior Lecturer at the Department of Electronic and Electrical Engineering, University of Sheffield, UK and from 2023 to 2024, a Reader at the School of Electronic Engineering and Computer Science, Queen Mary University of London (Visiting Professor from 2024). Since 2024, he has been a Professor at the Department of Electrical and Electronic Engineering, Hong Kong Polytechnic University. He has published 500+ journal and conference papers, six book chapters, and two research monographs titled "Wideband Beamforming: Concepts and Techniques" (Wiley, 2010) and "Low-Cost Smart Antennas" (Wiley, 2019), respectively. His research interests are mainly focused on sensor array and multichannel signal processing and its various applications, such as robotics and autonomous systems, human computer interface, radar, sonar, and wireless communications.

He is a member of the Applied Signal Processing Systems Technical Committee (Chair for 2026-2027) of the IEEE Signal Processing Society (SPS), the Digital Signal Processing Technical Committee (Chair for 2022-2024) of the IEEE Circuits and Systems Society, and the IEEE SPS Education Board (2024-2026, Chair of its Educational Conference Program Committee), and a former member of the Sensor Array and Multichannel Signal Processing Technical Committee of the IEEE SPS (Chair for 2021-2022), the IEEE SPS Technical Directions Board (2021-2022), and the IEEE SPS Conference Board and its Executive Subcommittee (2022-2023). He also acted as an associate editor for IEEE Trans. on Signal Processing, IEEE Access, and Journal of the Franklin Institute, and an Executive Associate Editor-in-Chief of the journal Frontiers of Information Technology and Electronic Engineering; currently he is an associate editor for IEEE Transactions on Circuits and Systems I: Regular Papers and IEEE Antennas and Wireless Propagation Letters. He is an IEEE Distinguished Lecturer for the Aerospace and Electronic Systems Society (2023-2026).

Haiyang Zhang (M'17) received the B.S. degree in communication engineering from Lanzhou Jiaotong University, Lanzhou, China, in 2009, the M.S. degree in information and communication engineering from the Nanjing University of Posts and Telecommunications, Nanjing, China, in 2012, and the Ph.D. degree in information and communication engineering from Southeast University, Nanjing, China, in 2017. From 2017 to 2020, he was a Postdoctoral Research Fellow with the Singapore University of Technology and Design, Singapore. From 2020 to 2022, he was a Postdoctoral Research Fellow with the Weizmann Institute of Science, Israel, where he was awarded the FGS Prize for outstanding research achievements. He is currently a Full Professor with the School of Communications and Information Engineering, Nanjing University of Posts and Telecommunications. His research interests include 6G near-field MIMO communications, deep learning, and sampling theory. He received the IEEE Marconi Prize Paper Award in Wireless Communications in 2025. He is/was the Co-Chair of the IEEE ICC Workshop on 6G Near-Field Communications. He served as a Guest Editor for the IEEE Internet of Things Journal, IEEE Transactions on Cognitive Communications and Networking, and IEEE Transactions on Aerospace and Electronic Systems. Currently, he is an Associate Editor of IEEE Wireless Communications Letters.

Yonina C. Eldar (S'98–M'02–SM'07–F'12) is the Aoun Chair Professor of Electrical and Computer Engineering at Northeastern University and the Dorothy and Patrick Gorman Professorial Chair of Mathematics and Computer Science at the Weizmann Institute where she founded and heads the Signal Acquisition Modeling Processing and Learning Lab (SAMPL) and the Center for Biomedical Engineering. She is also a Visiting Professor at MIT and Princeton, a Visiting Scientist at the Broad Institute, and an Adjunct Professor at Duke University and was a Visiting Professor at Stanford. She is a member of the Israel Academy of Sciences and Humanities and of the Academia Europaea, an IEEE Fellow and a EURASIP Fellow. She received the B.Sc. degree in physics and the B.Sc. degree in electrical engineering from Tel-Aviv University, and the Ph.D. degree in electrical engineering and computer science from MIT. She has received many awards for excellence in research and teaching, including the Israel Prize (2025), Landau Prize (2024), IEEE Signal Processing Society Technical Achievement Award (2013), the IEEE/AESS Fred Nathanson Memorial Radar Award (2014) and the IEEE Kiyo Tomiyasu Award (2016). She received the Michael Bruno Memorial Award from the Rothschild Foundation, the Weizmann Prize for Exact Sciences, the Wolf Foundation Krill Prize for Excellence in Scientific Research, the Henry Taub Prize for Excellence in Research (twice), the Hershel Rich Innovation Award (three times), and the Award for Women with Distinguished Contributions. She was selected as one of the 50 most influential women in Israel, and was a member of the Israel Committee for Higher Education. She is the Editor in Chief of Foundations and Trends in Signal Processing, a member of several IEEE Technical Committees and Award Committees, and heads the Committee for Promoting Gender Fairness in Higher Education Institutions in Israel.